A Polarized ^{3}He Beam for Parity Violation Studies on the Princeton Cyclotron

David Aaron Siegel

Abstract

The use of a high-current polarized ^{3}He beam could facilitate a large number of nuclear physics measurements. One such experiment is a measurement of the meson exchange coupling constant f_π, which could be accomplished through the examination of the radiative decay of polarized excited ^{19}Ne, produced through collisions of polarized ^{3}He with ^{20}Ne. While polarized ^{3}He beams have been attempted in the past, the currents that they have produced on target have not been sufficient to obtain high quality data. However, given new technology in noble gas polarization we believe that currents of a few microamps of polarized ^{3}He can now be achieved. This thesis details the large steps made toward using a polarized ^{3}He beam to perform parity violation experiments, centering on the construction of such a beam. Although the time constraints inherent in this project precluded the completion of a polarized beam, significant progress was made in that direction. Measurements of the magnetic field present in the Princeton cyclotron were coupled with calculations that predicted flow rates and inhomogeneity effects to yield a complete characterization of the ^{3}He as it is injected into the cyclotron, including a theoretical value for the total polarization loss experienced by the gas from the time it leaves the pumping chamber until the time it enters the ionization chamber. These calculations were used to design and construct a model cyclotron system, which was then tested to determine the accuracy of the calculations. In doing this, we succeeded in creating one of the first flowing gas systems that was able to achieve a significant degree of polarization. The calculations and the design choices were almost completely borne out by experimental evidence. Although we were not able to see a signal from the gas leaving the system during the time in which this thesis took place, we expect to remedy this shortly with very little change to the system as it stands now. The polarized gas delivery system will then be ready for use in producing a high-current polarized ^{3}He beam for the Princeton Cyclotron.

Acknowledgements

I want to begin by thanking my advisor, Prof. Gordon Cates, for helping to teach me what is important in physics. This thesis would not have even gotten off the ground if not for the constant help and friendship of Paul Bogorad; I cannot begin to thank him enough. In the last few weeks, the willing aid of Mikhail Romalis, Brian Saam, and Christopher Erickson has made the difference between a failed experiment and a successful one, and I offer my heartfelt gratitude to them all. Lazlo in the machine shop and Mike in the glass shop built more of my apparatus than I did, and still managed to be friendly while doing it. It was a pleasure working with both of them. The beautiful color pictures of the aperture seen in figure 3.4 appear due to the help of Prof. Bob Austin, and Steve Kidner's voluminous knowledge of the cyclotron was absolutely invaluable in designing the apparatus. Bas, Karen, Hunter, and the rest in the atomic group have always been ready with helpful advice or a friendly joke, and the same holds true for Stan, Albert, and Adam in the nuclear group. Having labmates like these has made my stay here more pleasant. I would also like to thank Professors Kumar, Peebles, and Page for their advice and for their enthusiasm. Physics needs more professors like these.

My friends are what have made my four years here a time that I will always remember fondly. Thanks to Uday, Paul, Brian, and Tina. Your friendship and understanding have been bright spots in my life. Thanks for putting up with me the last few years. The same goes double for Arnab and Marc, since they've had to put up with me for even longer. I would especially like to thank Charlotte, who has not only been my friend almost since I arrived at Princeton, but has also made me very happy the past couple of years.

Finally, I would like to thank my mother, my father, my sister, my grandmother, and the rest of my family, without whom I would not be as happy as I am right now.

Contents

Chapter 1

Introduction

Parity non-conservation experiments have proven to be a useful tool in probing the validity of both the standard model and certain theoretical extensions of it. However, while much progress has been made in understanding leptonic and semileptonic weak interactions, hadronic weak interactions have not been characterized to a great degree. Parity non-conserving (PNC) nucleon-nucleon (N-N) interactions provide an important experimental tool for probing the effect that the strong force has upon weak interactions between quarks, but severe experimental difficulties have to date precluded a prolonged investigation into this area. Experiments using parity-mixed doublet states in ^{19}F and ^{18}F have yielded some pieces of the puzzle, like linear combinations of some relevant coupling constants such as f_π [2], but these experiments alone do not tell the whole story. There exist, however, measurements that could help clarify the field, yielding different combinations of the couplings that would allow for new progress to be made in puzzling out the effects of the strong force. For example, the radiative decay of a polarized excited state of ^{19}Ne can be used to study the PNC asymmetry in the gamma produced. Unfortunately, it has been difficult to produce a sufficient rate of the necessary polarized excited state of ^{19}Ne. However, recent advances have led us to believe that a high enough rate can be achieved through the creation of an intense laser polarized ^{3}He beam for the Princeton Cyclotron.

1.1 The Feasibility of a Polarized ^{3}He Beam

While polarized ^{3}He beams have been used in the past, for example, in the Texas A&M cyclotron during the mid 70's [12], two major factors have prevented the widespread utilization of this experimental tool. First of all, in all of these beams the gas was ionized prior to its introduction into the cyclotron system, a process whch required complicated apparatus. In contrast, simply introducing unpolarized ^{3}He through a capillary tube into an ionization chamber, and then into the cyclotron, requires no major alterations to the machine.

Even if this difficulty were ignored, a second and more serious problem with these beams arises, in that the currents that they produce are simply too low to obtain good statistics on certain nuclear physics measurements. The Texas A&M cyclotron [12] produced a current of 100 nA on target, at least an order of magnitude less than that required to achieve a reasonable level of sensitivity on the aforementioned ^{19}Ne measurement. These two difficulties have severely slowed the advance of research in this area, but a great deal of progress in the methods of polarized ^{3}He production has greatly enhanced the possibility of a successful polarized beam.

Our lab has repeatedly polarized large quantities of ^{3}He using the phenomenon of spin exchange between unpolarized ^{3}He and optically pumped rubidium vapor. These quantities of polarized gas have been used in a wide range of experiments, including the determination of the neutron spin structure function at the Stanford Linear Accelerator Center, where the polarization of ^{3}He in the target cell reached as high as 40% [4], and the magnetic resonance imaging of guinea pig lungs [13]. In the former experiment, the E142 collaboration demonstrated the ability to polarize a significant volume of gas (170 cc) at high pressure ($\sim$ 9 atm at room temperature);

other experiments in our lab have demonstrated as well the ability to hold this polarized gas with long lifetimes in glass cells similar to the ones used at SLAC. In the latter experiment, the highly polarized gas was passed through a tube into the guinea pig's lungs, retaining a significant degree of polarization in the process. Although the precise degree of depolarization during transport was not fully characterized, the fact that polarized ^{3}He can be transported in this manner is encouraging for the prospect of the injection system that we envision for the Princeton Cyclotron.

With improved versions of the technology utilized in the aforementioned experiments, we expect to be able to transport highly polarized ^{3}He into the cyclotron at a constant rate of 2 sccm. This translates into a beam current on the order of 1–5 μA, which should be sufficient to obtain excellent statistics in the ^{19}Ne experiment. In addition to bringing about an order of magnitude increase in the current, this method is also relatively easy to implement. Clegg has stated his belief that polarized ^{3}He can be ionized without significant depolarization from its passage through the ionizer [8]. If this turns out to be true, then the basic structure of the gas injection system would not need to be appreciably altered to accommodate a polarized ^{3}He beam. This improved current and relatively easy implementation combine to make a polarized ^{3}He beam for the cyclotron an attractive goal.

1.2   Experiments with a Polarized ^{3}He Beam

Now that we have examined the feasibility of a polarized ^{3}He beam, the physical motivation for why such a beam should be constructed must be provided. In addition to the ^{19}Ne experiment briefly mentioned above, a similar ^{21}Ne experiment is made possible through the construction of this beam, and an interesting astrophysics measurement can be performed as well.

1.2.1 The ^{19}Ne Experiment

The subject of weak interactions has been extensively studied over the past few decades. Many interesting and highly successful experiments have been accomplished characterizing both leptonic and semileptonic weak interactions, and these experiments have greatly limited the scope of possible theories that could describe this interaction. The $SU(2) \otimes U(1)$ electroweak unification theory has been tested again and again, and the mediator bosons $W^\pm$ and Z^0 that it predicts have been discovered. PNC interactions have been fundamental in many of these experiments. However, weak interactions between quarks have not been so widely studied. It is to be expected that the strong nuclear force between the quarks modifies the weak interaction in some way, but the way in which this modification occurs is not yet well understood. On the theoretical side, the lack of an easily calculable theory of strong interactions in the limit of low energies has made the problem difficult to solve. On the experimental side, studies of weak interactions between quarks can only be accomplished when some clean signature allows the effects of weak interactions to be picked out from the dominant effects of strong and electromagnetic interactions. Application of the theory shows that the only reasonable process that can yield significant insights into neutral-current weak interactions between quarks is the N-N weak interaction, where parity non-conservation provides just such a clean signature [2]. Unfortunately, experiments of this type have been fairly difficult to accomplish. Parity non-conservation in the weak interaction allows for a mixing of parity states, and this mixing causes a spatial asymmetry in the detection of the gamma released by the excited polarized ^{19}Ne, to use our example. However, in most cases this mixing requires the utilization of a complete sum over parity eigenstates to describe both the initial and the final states. As mentioned above, theoretical calculations of these nuclear states are not

at a sufficient level of accuracy to use in this manner, although there has been some recent progress in this area.

There is a way around this, though, if we confine our focus to transitions involving closely spaced parity doublets of the same spin but opposite parity. In this case, because of the $\frac{1}{\Delta E}$ dependence of the first order energy shift in perturbation theory, where ΔE is the splitting between the two levels of the parity doublet, 275 keV in ^{19}Ne, the sum over states described above reduces to a good approximation to a sum over only two states. Thus, the mixed states become, for the case of the $J^\pi = \frac{1}{2}^-$ excited state and the $J^\pi = \frac{1}{2}^+$ ground state with which we are dealing [2, eq. 13],

$$|i> = |\frac{1}{2}^- > + \epsilon|\frac{1}{2}^+ >, \tag{1.1}$$

$$|f> = |\frac{1}{2}^+ > - \epsilon|\frac{1}{2}^- >, \tag{1.2}$$

where

$$\epsilon = \frac{<\frac{1}{2}^+|V_{PNC}|\frac{1}{2}^- >}{\Delta E}. \tag{1.3}$$

We see that the V_{PNC} potential in (1.3) is what causes the splitting, and this potential arises due to the parity violating weak interaction.

As the weak interaction is virtually a contact interaction due to the large masses of the W$^\pm$ and the Z^0 mediating vector bosons, and as the repulsion between two nucleons prevents the quarks located therein from achieving a close proximity, it is somewhat difficult to use the weak-current formalism of the exchange of W and Z bosons as a calculative method. In light of this, a formalism has been created which utilizes the exchange of mesons to characterize hadronic weak interactions. Desplanques, Donoghue, and Holstein (DDH) have explained this theory, which centers around the exchange of either single mesons, like π, ρ, and ω, or multiple mesons, like $\pi\pi$ [9]. One nucleon vertex is calculated using the strong interaction, and the other using the weak interaction, as displayed in figure 1.1.
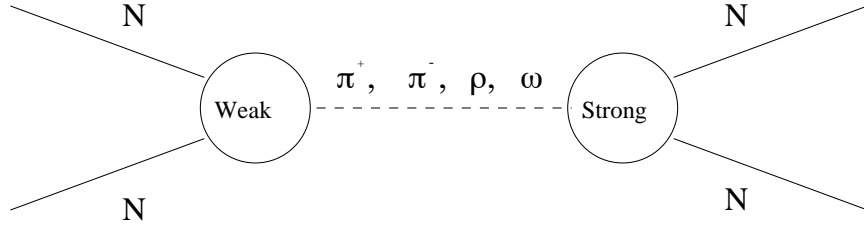
Figure 1.1: Simplified Feynman diagram of N-N interaction with meson exchange.

The PNC potential in (1.3) has been expressed by DDH in terms of this exchange of mesons [9]. Single meson exchanges of π, ρ, and ω dominate this potential, which is characterized by the coupling strengths f_π and h_ρ^0 in the case of the radiative decay of ^{19}Ne. The subscripts refer to the exchanged particles, and an experimental determination of these coupling strengths would provide a test of the meson exchange model and probe the effect of the strong force upon the hadronic weak interaction. Previous measurements of f_π in ^{18}F, which also has a closely spaced parity doublet, have yielded values of the coupling constant that fall toward the low end of the predicted range. However, other measurements of f_π, gained through comparisons of experiments using ^{21}Ne and ^{19}F, have yielded conflicting values of this coupling constant [5]. While there are studies of first forbidden beta decays in ^{18}Ne and ^{19}Ne which allow for a calibration of necessary nuclear matrix elements, thus making interpretation of the ^{18}F data relatively straightforward, no such calibration exists for the ^{21}Ne data [5]. While this confusion might be slightly allayed by a new experiment using ^{21}Ne, such as the one described in section 1.2.2, it is also possible that the disagreement stems from an inaccurate calculation of the nuclear wavefunctions. Thus, it would be beneficial to measure f_π without using ^{21}Ne.

We believe that a measurement using ^{19}Ne is an excellent way to make an accurate calculation of f_π. The relevant matrix elements for a ^{19}Ne experiment could

be calibrated using the aforementioned first forbidden beta decays, so no interpretation problem of the sort encountered with ^{21}Ne would occur. A measurement with ^{19}Ne would determine a linear combination of f_π and h_ρ^0, which could then be compared to the many existing measurements with ^{19}F, which yield a different linear combination of the two coupling factors. A highly accurate value of f_π could thus be determined. That this experiment has not already been performed is due to the difficulty in producing significant quantities of polarized excited ^{19}Ne. The production of a high-current polarized ^{3}He beam makes sufficient quantities possible.

Using the high-current ^{3}He beam, we would produce significant rates of polarized excited ^{19}Ne through the reaction ^{20}Ne$(^3\vec{\text{He}}, \alpha)^{19}\vec{\text{Ne}}^*$. We expect high polarizations of ^{19}Ne based upon the findings by Adelberger *et al.*, which states that the similar reaction ^{22}Ne$(\vec{\text{p}}, \alpha)^{19}\vec{\text{F}}^*$ efficiently produces polarized ^{19}F* nuclei [3]. The $J^\pi = \frac{1}{2}^-$ excited state of ^{19}Ne that is thus produced undergoes radiative decay, releasing a gamma ray of 275 keV in decaying to the other state in the parity doublet, $J^\pi = \frac{1}{2}^+$. If parity were conserved the released gamma would be emitted in equal proportions both parallel and anti-parallel to the polarization axis, but the PNC potential due to the weak interaction mixes the two states of the parity doublet in the manner described in (1.2, 1.3), causing a spatial asymmetry in the direction of gamma emission. The emitted gammas could be measured by using detectors along both sides of the polarization axis, and the sign of the polarization could be flipped frequently to minimize statistical error. We believe that, using this method, the rate of gamma detection would be sufficiently high that the data extracted from this asymmetry measurement could be combined with that of the ^{19}F measurements to yield an accurate value of f_π and thus clarify the field significantly.

1.2.2 The ^{21}Ne Experiment

As mentioned previously, an accurate measurement of the gamma asymmetry in the radiative decay of polarized excited ^{21}Ne would be of use in checking the degree of disagreement among measured values of f_π. Such an experiment could be accomplished very cleanly using the high-current polarized ^{3}He beam. The reaction ^{22}Ne($^3\vec{\text{He}}, \alpha)^{21}\vec{\text{Ne}}^*$ could be used to produce large rates of polarized excited ^{21}Ne. The ^{21}Ne undergoes radiative decay, emitting a 2.8 MeV gamma ray when the $\frac{1}{2}^-$ excited state, which is mixed with the $\frac{1}{2}^+$ parity doublet state, decays to the $\frac{3}{2}^+$ ground state. As in the case of the ^{19}Ne experiment, the relative frequency of emitted gamma rays either parallel or anti-parallel to the polarization direction could be measured, and an asymmetry computed. This experiment would be easier to accomplish however, as the two parity doublet states are separated by only 5.7 keV. This smaller separation causes a greater degree of mixing between the states and thus leads to a large enhancement of the PNC gamma asymmetry. While the ^{19}Ne experiment is still preferred, due to the availability of the aforementioned beta decay calibration method for the relevant matrix elements, a ^{21}Ne asymmetry measurement could provide a good first test of the polarized ^{3}He beam, in addition to yielding some interesting physics.

1.2.3 Production Mechanisms for ^{27}Al in Nuclear Astrophysics

Besides its use as an important tool in measurements involving PNC N-N interactions, the polarized ^{3}He beam can also be utilized in nuclear astrophysics experiments. Studying production mechanisms for ^{27}Al aids in understanding both the interstellar abundance of ^{26}Al and some abundance anticorrelations in globular clusters. One production mechanism is the reaction ^{26}Mg(p, $\gamma)^{27}$Al, which has a resonance at 90

keV in the center of mass. Unpolarized ^{3}He is ordinarily used to study this reaction, but these studies are cluttered by the reaction $^{16}O(^3He, d)^{17}F$, which has an s-wave resonance. However, if the $^{26}Mg(p, \gamma)^{27}Al$ resonance is p-wave, then a polarized ^{3}He beam could be used to more cleanly study the reaction.

1.3 The Construction of a Polarized ^{3}He Beam

Having motivated the creation of a polarized ^{3}He beam, and at least partially established its feasibility, we should briefly discuss what we hope to accomplish with this thesis. Although it would have been almost impossible to setup a working polarized beam in the time allotted, our goals for this thesis are almost as ambitious. By the completion of this project we hope to have built and tested a working prototype of the gas delivery system. In order to make this a reality, it will be necessary to understand both the practical and the theoretical design requirements of the polarized beam. After a design has been put forth, we will proceed to construct the system, and then test it in a situation that mimics the cyclotron setting as closely as possible.

Chapter 2

The Pumping Chamber

The design of the polarized ^{3}He injection system separates neatly into the following two major areas: the design of the pumping chamber, and the design of the gas handling system. The design of the pumping cell, which will be discussed in this chapter, centers on issues regarding optical pumping and spin exchange, and involves optimization of laser output, allowance for sufficient pump-up time on average, and minimization of spin-relaxation rate. The design of the gas handling system is the subject of chapter three, and involves issues of gas flow, including regulation and minimization of spin-relaxation.

A great deal of work has been done to further the understanding of issues surrounding the creation and maintenance of highly polarized noble gas cells; the design of the pumping chamber that is to be used in the ^{3}He injection system builds upon the efforts involved in performing the aforementioned SLAC and magnetic resonance imaging experiments [4, 13]. The recent inclusion of diode laser arrays into the field, which can produce 7 times more laser power than the 5 Ti:Sapphire lasers that were used in the E142 experiment for about seventy times less money, has also had a significant effect upon the design of the chamber.

2.1 A Discussion of Optical Pumping and Spin Exchange

In order to understand the specifics of the cell design, it is necessary first to understand the requirements of the method of ^{3}He polarization that we are using, which is the collisional spin exchange of ^{3}He with optically pumped rubidium vapor.

2.1.1 Optical Pumping of Rb Vapor

In order for optical pumping with rubidium to occur, the cell must first contain a significant density of rubidium vapor. Thus, the first design requirement of the cell is that it must be able to handle the inclusion of a minimum of 100 mg of rubidium, some of which will be converted to a vapor during operation. The fact that there will be relatively large amounts of liquid rubidium in the cell means that the geometry of the cell's output port cannot make it easy for the rubidium to leave the cell via this port, as most of the liquid rubidium would quickly run out of the cell, making it impossible to polarize the ^{3}He . Thus, the conductance of the output port must be low with respect to the liquid, which can be accomplished by making it gravitationally unfavorable for the liquid to enter the output port. Obtaining a significant number density of rubidium vapor (on the order of 10^{14} cm^{-3}) requires that the temperature of the cell be approximately 180 ^{0}C. The cell therefore requires an oven, which must be designed so as to allow for the exit of both the input and the output ports of the cell, as well as for the entrance of the laser light.

The ground state of the valence electron in the rubidium vapor is $5S_{\frac{1}{2}}$, where $m_J = \pm\frac{1}{2}$. The first excited state of the electron is $5P_{\frac{1}{2}}$ and it is separated from the ground state by 795 nm. Tuning the diode laser to this line, which is called the

D1 absorption line, induces the electron to make the transition to the excited state. We should note that the hyperfine splitting due to the interaction of the nuclear and electronic spins has been neglected as, at 3036 MHz, it is much less than the line-width of the diode laser [7]. If the light is circularly polarized with a positive helicity, and a small magnetic field of a few gauss is applied to set a polarization axis, than the $\Delta m_J = +1$ selection rule implies that only electrons in the ground state with $m_J = -\frac{1}{2}$ can make the transition to the excited state. Once in the excited state, the electron radiatively decays back into either of the two ground states, leading to a build-up of the $m_J = +\frac{1}{2}$ ground state. In this way the valence electron of the rubidium acquires a polarization over time. Unfortunately, the light radiated in this decay is unpolarized and can cause severe relaxation of the rubidium. In order to eliminate this problem, a buffer gas of N_2 must be included in the cell. This gas collides with the rubidium, which then decays non-radiatively, giving up its energy to the nitrogen molecule. In our lab, we have found that 70 to 100 Torr of nitrogen in a ten-atmosphere cell is sufficient to accomplish this non-radiative quenching. This method of polarization accumulation is known as depopulation pumping and is displayed graphically in figure 2.1. The mixing referred to there is due to the fact that collisions with N_2 effectively mix the excited states of the electron.

Rubidium vapor that has already been polarized will no longer absorb laser light. Since the spin destruction rate is, in general, much slower than the optical pumping rate, the rubidium polarization within a given absorption length is very nearly 100% [7], as long as there is sufficient laser power left to optically pump the vapor. The length of the cell along the laser is thus dependent on the laser power, since, once the flux of laser light drops to an insufficient level, the polarization drops to almost zero within a few millimeters. Due to the high power of our new diode laser array, we have chosen to use a cylindrical cell of volume equal to approximately 285 cc,

Collisional Mixing

$m_J = -1/2$ $m_J = +1/2$

$5P_{1/2}$

Radiaitve and
Non-radiative
Decay

σ^+

Radiaitve and
Non-radiative
Decay

$5S_{1/2}$

$m_J = -1/2$ $m_J = +1/2$
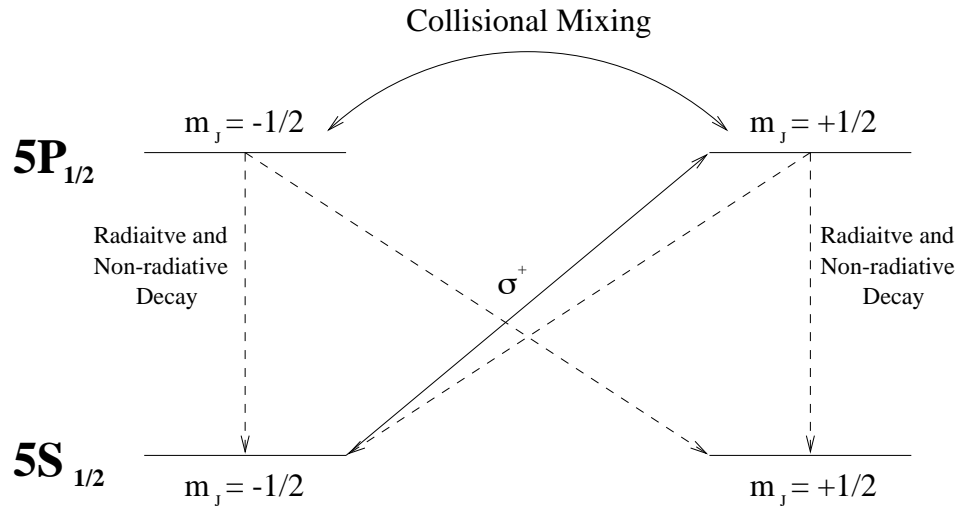
Figure 2.1: Depopulation Pumping of Rubidium in the Presence of an N_2 Buffer Gas

which is significantly larger than the cells used previously. Optics will spread the light to illuminate all of the 5.5 cm inner diameter of the cell. In order to make sure that enough of the 120 Watts of laser light is absorbed by the rubidium throughout the 12.0 cm length of the cell, the chamber must be kept at a pressure of nearly 15 atmospheres when running. The concomitant increase in the number density of rubidium causes a significant pressure broadening of the D1 line, which allows more of the light from the diode laser, which has a very broad spectral distribution, to be utilized.

2.1.2   Spin Exchange with Optically Pumped Rubidium

The theory of collisional spin exchange has been elucidated in a detailed article by Happer *et al.* [11]. As most of the relevant design issues resulting from this form of polarization have been covered in the preceding discussion of optical pumping, we will only give a brief discussion of spin exchange here.

^{3}He is polarized through collisions with optically pumped rubidium vapor. In a given collision there is a very small, although non-zero, probability that the wavefunction representing the valence electron of the rubidium will overlap with the nucleus of the ^{3}He , and that the resulting hyperfine interaction between the spin of the electron and the nuclear spin, given by

$$\mathcal{H} = \frac{16\pi}{3} g_n \mu_n \mu_b (\vec{K} \cdot \vec{S}) \psi_e^2 (\vec{r} = 0), \tag{2.1}$$

will induce a spin-flip in both the electron and the ^{3}He nucleus, effectively exchanging the two-spins. As the cross-section for the process of spin exchange is only $\sim 10^{-24}$ cm^2 [10], the slight depolarization that the exchange causes in the optically pumped rubidium is not significant, since the rate for optical pumping is much faster than the rate for spin-exchange. The slow rate of spin-exchange means that, if high ^{3}He polarizations are to be obtained, the spin-relaxation rate of the polarized ^{3}He must be even slower.

If we define the spin-exchange rate γ_{SE} as

$$\gamma_{SE} \equiv \langle \sigma_{SE} v \rangle [\text{Rb}], \tag{2.2}$$

and denote the relaxation of ^{3}He due to any means other than spin-exchange by Γ_1, then the polarization of ^{3}He at any time is given by

$$P_{^3He}(t) = \langle P_{Rb} \rangle \left(\frac{\gamma_{SE}}{\gamma_{SE} + \Gamma_1} \right) \left(1 - e^{-(\gamma - SE + \Gamma_1)t} \right), \tag{2.3}$$

where $\langle P_X \rangle$ refers to the polarization of X. Since, as mentioned above, the rubidium polarization is nearly 100%, the major limiting factor to ^{3}He polarization is the relaxation of ^{3}He , which has contributions from the following major areas:

1. ^{3}He - ^{3}He binary collisions.

2. Interaction with the walls of the pumping chamber.

3. Magnetic field inhomogeneities.

4. Collisions with paramagnetic gaseous impurities.

The minimization of these factors has been the goal of a great deal of work, and we will use the wisdom of those who have gone before us. The cell is made from Pyrex glass, which, while not the ideal material out of which to make the cell due to the fact that helium can leak through it, should provide long enough relaxation times for our purposes, while having the benefit of being easier to work with than the alternative aluminosilicate glass that was used in the E142 experiment. The effect of magnetic field inhomogeneities can be limited by applying a stronger constant magnetic field than would be needed for the purposes of optical pumping alone. It can also be limited by increasing the pressure of the cell. While this form of relaxation is not expected to be important in the high pressure pumping chamber, it will become very important in gas transport, as will be described in section 3.2.3. ^{3}He - ^{3}He collisions cannot, unfortunately, be limited, but gaseous impurities can be severely curtailed through some of the purification processes that will be described in the next section. Given reasonable relaxation rates, we expect a spin-up time on the order of 4 hours and a maximum polarization around 30 - 50%.

2.2 Construction of the Chamber

As stated above, the pumping chamber is a cylindrical cell, made from Pyrex glass, with an inner diameter of 5.5 cm and a length of 12.0 cm along the path of the laser light. The wall thickness is 4 mm, and initial pressure tests of the cell have given a good indication that the cell can handle the $\sim$ 15 atm of pressure that it will experience while in operation. There are a total of three ports on the cell, as can be

seen in the diagram of the chamber given in figure 2.2. The first port is for attachment of the cell to the vacuum system, and does not end in a valve. Also connected to the vacuum system at this time are the two rubidium reservoirs, shown to the right in figure 2.2. Approximately one gram of rubidium is placed in the larger reservoir, which is then sealed off. The cell is heated to ~ 300 ^{0}C while under high vacuum in order to out-gas any impurities present in the chamber. After this process, the rubidium is distilled into the smaller reservoir using a hand-held torch. The initial reservoir is then pulled off of the system. At this point, while the cell is still at high temperature, argon gas is sent through the chamber via the input and the output ports shown in the diagram in order to purge the cell of remaining impurities. The oven heating the chamber is then removed, and rubidium is distilled into the cell itself using a torch. This two-stage distillation process is thought to reduce the amount of impurities that are present in the rubidium. After this is completed, the cell is pulled off of the vacuum system.

The input and output ports, shown respectively on the left and on the right in figure 2.2, connect the chamber to the gas handling system. Each port is bent so as to minimize the flow of rubidium out of the cell during operation. Each tube is connected to a glass-to-metal seal, and the non-magnetic stainless steel present in the output port is gold plated in order to minimize depolarization due to wall relaxation. The tubes exiting the chamber are also highly constricted, with an inner diameter of 1.0 mm, in order to lessen their conductance and to help prevent the polarized gas from coming into contact with the valves, made respectively from non-magnetic stainless steel and glass, which close off the cell from the gas handling system. The gas used during operation is pre-mixed, containing 99.25% ^{3}He and 0.75% N_2. During operation, the cell is surrounded by an oven made from high-temperature plastic, which operates by passing heated air around the cell. Windows in the oven allow

Side View

Metal Valve

Bellows

Glass Valve

Glass-to-Metal Seal

6.3 cm

8.5 cm

12.0 cm

Rubidium
Reservoir

Front View

3.8 cm
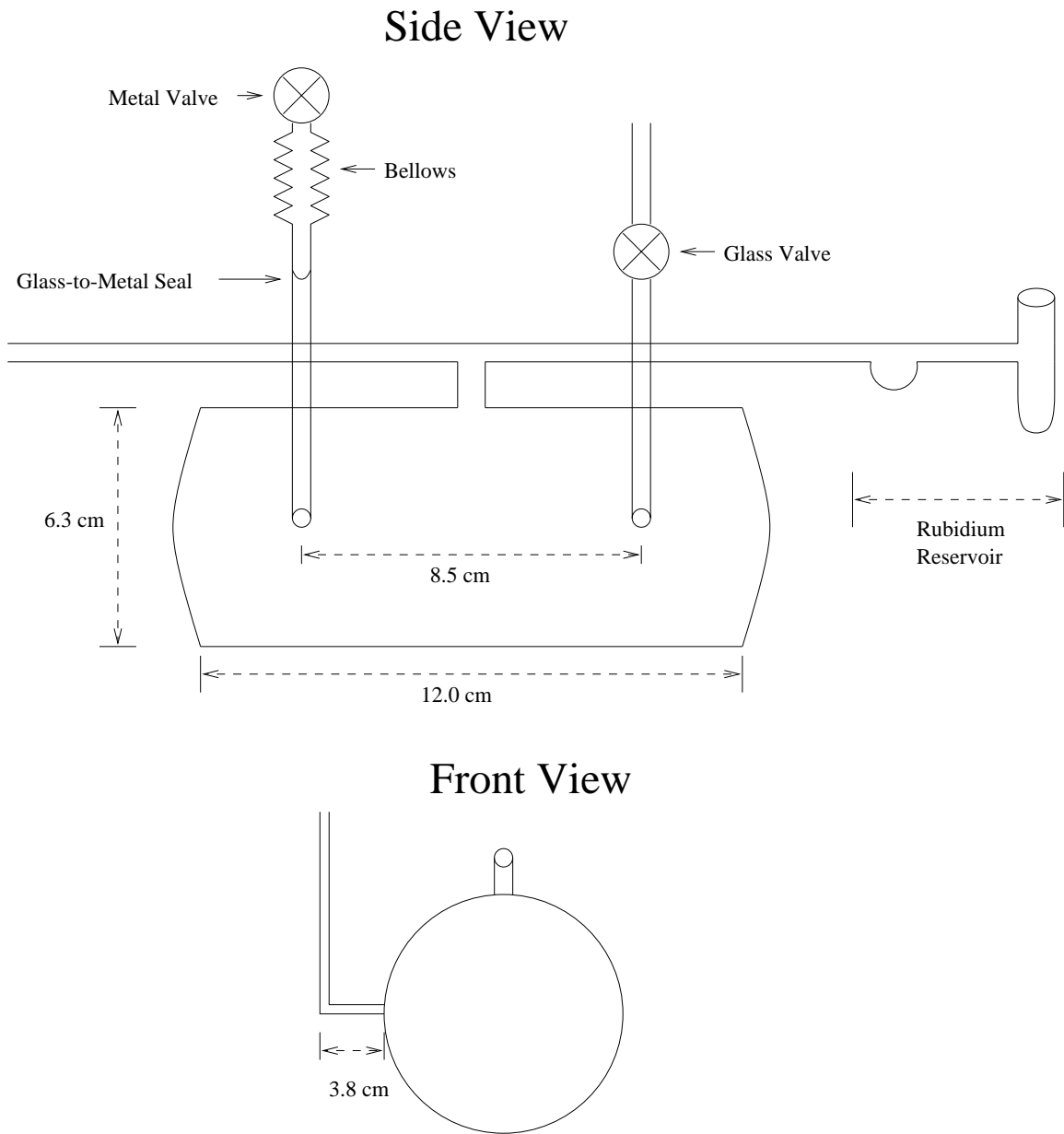
Figure 2.2: Diagram of the Pumping Chamber while Connected to the Vacuum System.

laser light from the diode laser array to pass through the cell. Finally, Helmholtz coils surround the pumping chamber, providing the necessary 30 Gauss magnetic field. The design of the cell thus seeks to maximize the polarization of ^{3}He by minimizing the depolarizing factors described above. The use of the pumping chamber in tests of ^{3}He depolarization is described in chapter five.

Chapter 3

The Gas Handling System

Just as the form of the chamber is constrained by the requirements of optical pumping and spin exchange, the design of the gas handling system is shaped by the laws of gas flow and the desire to minimize depolarization in transport. However, unlike with the cell, these issues, as they relate to design specifications, have not been fully clarified. While polarized noble gases have been used in a flowing system before, notably in the aforementioned medical imaging work, the depolarization caused by the motion of the gas has not been fully characterized. As the loss of polarization during the passage of the gas from the cell to the cyclotron ionizer is likely to be one of the greatest obstacles to overcome, much of the work involved in this thesis has gone into creating a gas handling system designed with the express purpose of minimizing depolarization as much as possible, while simultaneously meeting the constraints of both the cyclotron and the pumping cell.

3.1   Gas Flow and Pressure Determination

The most basic requirement of the gas handling system is that it deliver gas to the cyclotron at a mass flow rate of 2 sccm, which is equivalent to a volumetric flow rate of 2 cc per minute at one atmosphere. The Princeton cyclotron can handle flow

rates between the extremes of 0.5-3.0 sccm, and the value of 2 was chosen because it allows for a safe margin of error while giving a sizeable beam current. While it is not difficult to design a system that is constrained in this way, the requirements of optical pumping make the task much more difficult. The cell must operate at a pressure of approximately 15 atmospheres. However, the ionization chamber in the cyclotron runs at a pressure of ~ 0.1 Torr. This is a huge pressure differential, and it requires drastic measures in order to satisfy both this difference and the necessary flow rate. Before we come upon the solution to this problem, though, we first need to truly understand just how great an obstacle it is.

3.1.1 Flow through a Tube

In examining the flow of gases, we find that there are two central concepts which will be of use to us. These are the notions of throughput and conductance, and they are related by the simple formula

$$Q = C\Delta P. \tag{3.1}$$

The throughput, Q, is a measure of the mass flow rate through a system, while the conductance, C, describes the volumetric flow rate as determined from the geometry of the system and the basic gas laws. If the temperature is constant throughout a system, then the throughput will also be constant at every point in the system. From (3.1) we see that, as $Q = C_A(P_2 - P_1) = C_B(P_3 - P_2)$ for two tubes of conductances C_A and C_B in series, $\frac{1}{C_{eq}} = \frac{1}{C_A} + \frac{1}{C_B}$. Thus, conductances in series add as resistances in parallel. Given a specified geometry, a starting pressure, and a constant throughput, it is therefore possible to work backwards and determine the pressure, not only at the top of the geometry, but at every point within it as well. As luck would have it, we know all three of these things.

As stated above, the desired throughput is 2 sccm, and the pressure in the ionization chamber, which is located at the beginning of the geometry, is ~ 0.1 Torr. The geometry too is somewhat fixed by the form of the area around the Princeton cyclotron. Leading into the ionization chamber from the outside is a tube of $\frac{1}{16}$ inch inner diameter. While it is possible to alter the diameter of this tube by threading a smaller diameter tube into it, the length of this tube, which is 36 inches, is essentially fixed. In the simplest geometry that we considered, this tube would simply be connected to a capillary tube that runs directly into the cell. Looking at the passage of gas through the system in reverse we start with a small volume at 0.1 Torr, then pass through an aperture into a fixed length of tube, move through another aperture into a capillary tube, and finally travel through a third aperture into the pumping chamber. A diagram of the geometry, along with the names by which we will henceforth refer to each section of it, is given in figure 3.1.

The study of gas flow is separated into the three basic regimes of viscous, intermediate, and molecular flow, with viscous flow being further subdivided into laminar and turbulent motion. In order to begin the calculation of the pressures at each point in the tube, which will be useful both in determining the pressure at the top of the tube and in determining the polarization loss due to magnetic field inhomogeneities, as will be described in section 3.2.3, we must have at least a vague notion of which regime holds in each section of tube. Such knowledge can be gained by examining the ratio of the diameter of the tube to the mean free path of the gas molecules, which is defined [14, eq. 2.57] as

$$\lambda = \frac{2.33 \times 10^{-20}T}{\xi^2 P(1 + \frac{79}{T})} \quad \text{cm,} \tag{3.2}$$

where T is the temperature, ξ is the molecular diameter in cm, and P is the pressure in torr. The molecular diameter of ^{4}He is 2.61×10^{-8} cm, and ξ for ^{3}He can be

To output valve on cell

Aperture Leading
from Cell into
Capillary
(will be small)

Capillary
Tube

Elbow between
Capillary and
Fixed Length
Tubes

Aperture into
Ionization
Chamber

Fixed Length Tube (36")
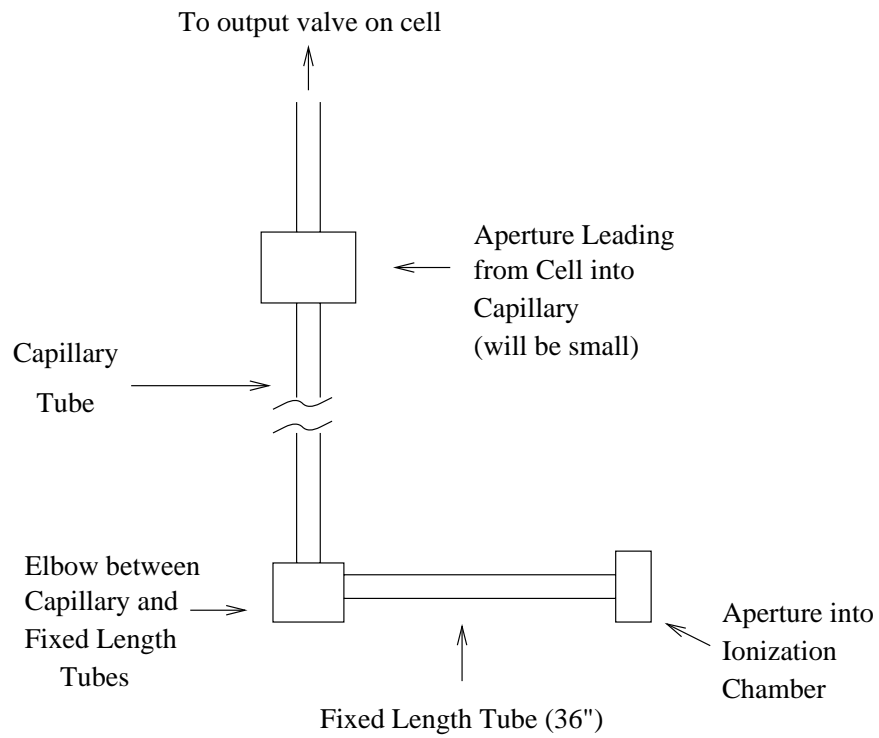
Figure 3.1: Make-up of the Gas Handling System from the Pumping Chamber to the Ionization Source (Not to Scale).

approximated as being the same as this value. At room temperature then, we have that

$$\lambda \simeq \frac{0.0131}{P} \ \text{cm}. \tag{3.3}$$

Molecular flow is dominant in cases where the mean free path of the gas is on the order of the diameter of the tube, so this regime should be utilized when $\frac{D}{\lambda} < 1$, where D is the diameter of the tube in cm. In the molecular flow regime, the motion of the gas molecules is governed primarily through collisions with the walls. In contrast, viscous flow occurs when the diameter of the tube is significantly greater than the mean free path of the gas, or when $\frac{D}{\lambda} > 110$ [14]. During the laminar phase of viscous flow, the primary determinant of the motion of the gas molecules is the viscosity of the gas. Different layers of gas tend to form in the tube, with the gas in the center of the tube moving swiftly, while the gas at the walls of the tube barely moves at all.

As the flow rate of the gas increases past that of laminar flow, the gas can enter a turbulent phase. This is a little understood transition, and it is fortunate that none of our work will breach the wall between laminar and turbulent flow. However, we are not free of all difficulties. Between the molecular and viscous flow regimes lies the almost equally confusing realm of intermediate flow. Here the gas shares characteristics with both the molecular and the laminar flow regimes, and it is, consequently, much more difficult to describe this type of flow quantitatively. As will be seen below, we are unfortunate in that a substantial distance of our fixed length of tube is likely to lie in the intermediate range.

As suggested above, we begin our determination of pressure at the point at which the gas is injected into the cyclotron. Moving from the ionization chamber into the first tube requires that the gas pass through an aperture, as seen in figure 3.1. As we are assuming a pressure of 0.1 Torr in the ionization chamber, and as the diameter

of the aperture, determined by the diameter of the tube present in the fixed length, is at most 0.16 cm, from (3.3) we see that the gas flowing through this aperture is in the molecular flow regime. Thus, we must utilize the equation for molecular flow through an aperture, taken from [14, eq. 3.72],

$$Q = 3.64(P_1 - P_2)(T/M)^{\frac{1}{2}} \frac{\pi D^2}{4} \quad \frac{\text{liter}}{\text{sec}}, \tag{3.4}$$

where P_2 and P_1 are the downstream and upstream pressures respectively, M is the molar mass of the gas, and D is the diameter of the tube. Although we are working backward through our geometry, we will keep the convention that P_2 represents the low pressure, or downstream end of the system, while P_1 represents the high pressure, or upstream end. From (3.4) we extract the upstream pressure, which is the pressure at the other end of the aperture.

Depending on the diameter of the tube used for the fixed length, the section of tubing just upstream from the first aperture may be in the viscous, the molecular or the intermediate regime. As the pressures we obtain by using the equations representing each flow regime can be widely divergent, it becomes necessary to determine the governing regime at every point. This would be extraordinarily time consuming without the use of a computer, and so a program has been written in order to make this and many other calculations much easier. As the program grew in size, its scope widened as well, and the finished code, which was written in C, performs all of the pressure calculations at every point in the geometry, with each point defined as a spot at which a measurement of the magnetic field was made. This definition was chosen because the program also calculates the total depolarization experienced by the gas due to magnetic field inhomogeneities as it travels down the tube. A full description of this aspect of the program can be found in section 3.2.3, and a complete listing of the program is located in appendix A.

The computer program determines which regime each point is in by looking at the pressure at the point before it and comparing this pressure to the pressure at the molecular-viscous intersection point, defined in [14, eq. 3.227] as

$$\bar{P}_i = \frac{116(T/M)^{\frac{1}{2}}\eta}{D} \quad \text{torr}, \tag{3.5}$$

where η is the viscosity of the gas in poises, T is in kelvin, D is in cm, and M is in grams per mole. As a good reference for the viscosity of ^{3}He could not be found, we were forced to approximate by scaling from the viscosity value of 186.0 micropoises that is given in [1] for ^{4}He at 273.14 K. This scaling was accomplished with the aid of [14, eq. 2.72],

$$\eta = \frac{0.998}{\pi\xi^2} \frac{\left(\frac{Mk_BT}{\pi}\right)^{\frac{1}{2}}}{\left(1 + \frac{79}{T}\right)} \quad \text{poises}, \tag{3.6}$$

where k_B is Boltzman's constant, and the other variables are in the same units as before. Scaling by the square root of the mass ratio between the isotopes of helium gives

$$\eta = \frac{12.570 \times 10^{-6}\sqrt{T}}{\left(1 + \frac{79}{T}\right)} \quad \text{poises}. \tag{3.7}$$

The reason that (3.6) was not just used directly to calculate the viscosity is that [1] gives a significantly different value of η than (3.6) yields and, given the uncertain nature of gas flow calculations in general, it was preferable to side as close as possible with experimental facts.

If the pressure at the point downstream of the position at which we are looking in the tube is more than ten times greater than (3.5), then the gas at the upstream position is in the viscous flow regime. Accordingly, the equation for viscous flow through a tube is used to calculate the pressure at this new position. We rearrange [14, eq. 3.53] to yield the formula

$$P_1 = \sqrt{\frac{192.15Q\eta L}{\pi D^4} + P_2^2} \quad \text{torr}, \tag{3.8}$$

where L is the length of the tube in cm, Q is in torr·liter/sec and, as before, P_1 is the upstream pressure. On the other hand, if the pressure at the point downstream of it is more than ten times less than (3.5), then the equation presenting molecular flow is used. Solving [14, eq. 3.93] for P_1, we obtain the formula

$$P_1 = P_2 + \frac{QL}{3.81(T/M)^{\frac{1}{2}}D^3} \quad \text{Torr.} \tag{3.9}$$

Finally, if the pressure at the point before it lies within these two extremes, the point in question lies within the intermediate gas flow regime. In this case, the following transcendental equation represents the dynamics of the gas flow [14, eq. 3.233]

$$Q = C_{mo}\bar{P}_i(\frac{1}{2}\delta^2 + \frac{17}{21}\delta + .009\log{(1 + 21\delta)}) \quad \frac{\text{liter}}{\text{sec}}, \tag{3.10}$$

where $\delta = \frac{P_2 + P_1}{2\bar{P}_i}$, $C_{mo} = \frac{3.81(T/M)^{\frac{1}{2}}D^3}{L}$, $\bar{P}_i$ is given by (3.5), and the downstream pressure is assumed to be negligible. The fact that the downsteam pressure is not always negligible introduces a fair amount of error into the calculation, but, if we choose a fixed length tube with a sufficiently small diameter, we can cause much of this tube to lie in the viscous flow regime, preventing undue accumulation of error due to multiple intermediate flow calculations. Of course, a better description of intermediate flow would be preferred over this approximation, but one could not be found. As (3.10) cannot be solved analytically for P_1, the computer program solves it numerically by making continually closer approximations to the root of the equation $Q - 2(\text{std.})\text{cc}/\text{min} = 0$ until an accuracy of better than 10^{-6} % is reached. Each point is examined in this manner until the top of the fixed length is reached, at which point it becomes useful to apply certain simplifications to the problem.

The connection between the fixed length and the capillary tubes, although technically an elbow due to the form of the cyclotron source, can be approximated by a simple aperture. As the pressure at the point of connection is already relatively

high for most reasonable values of the diameter of the tube in the fixed length, so that the motion of the gas is dominated by collisions among gas molecules and not between gas molecules and the walls of the tube, this approximation has little effect upon the pressure at end of the elbow. As before, which of the three regimes is used is dependent upon the value of the pressure at the point downstream of the connection, and the nature of this dependence is identical to that detailed above. If the point downstream of the aperture is in the molecular flow regime, which is almost impossible, then (3.4) describes the pressure at the other end of the aperture. In the more likely event that the aperture is in the viscous flow regime, the equation for viscous flow through an aperture [14, eq. 3.30-1] can be solved for the input pressure to yield the formula

$$P_1 = \frac{P_2}{2} + \frac{\left(4P_2^3 Q^5 (\frac{5T}{M})^{\frac{5}{2}} (2.0325 D^2 \pi)^5 + P_2^8 (\frac{5T}{M})^5 (2.0325 D^2 \pi)^{10}\right)^{\frac{1}{2}}}{2P_2^3 (\frac{5T}{M})^{\frac{5}{2}} (2.0325 D^2 \pi)^5}, \qquad (3.11)$$

where all of the variables are in the same units that are given above. Finally, if we are unlucky enough that the connection lies in the intermediate flow regime, we can only approximate the pressure at the other end of the aperture by taking the average of the results obtained from (3.4) and (3.11).

On the other side of the elbow is the capillary tube. For all reasonable values of the diameter of the fixed length, where reasonable values are defined as those which give acceptable polarization losses, this tube lies squarely within the viscous flow regime. Thus, we can simply calculate the pressure at each point using (3.8). This takes us to the top of the capillary tube, which connects to the cell via one final aperture. Figure 3.2 is a plot of the pressure of the gas as a function of its distance down the geometry of the system, where these pressures were obtained through the calculations described in this section. The distance denoted as -100 cm on the plot corresponds to a point well within the capillary tube, and the fixed length tubing
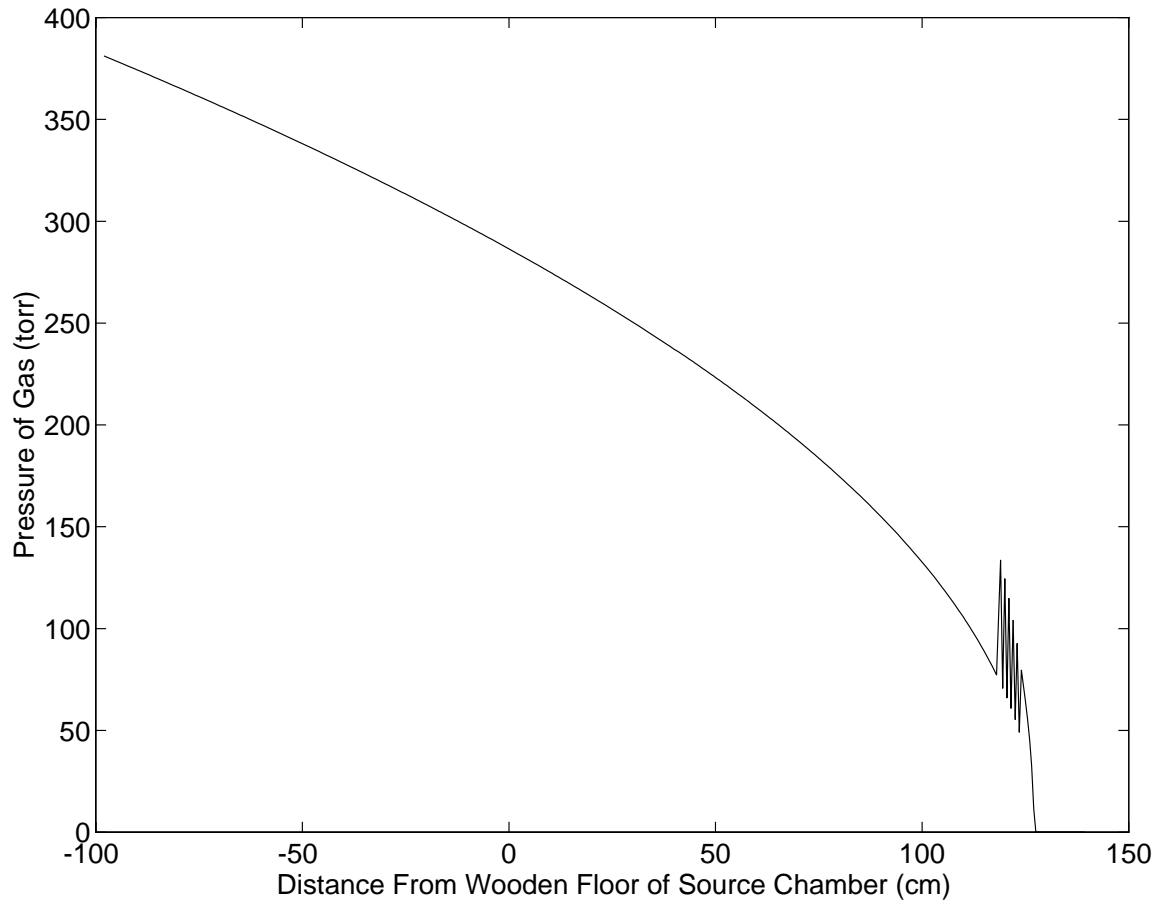
Figure 3.2: Plot of Pressure of Gas versus Distance from Wood Floor of Source Chamber.

runs until a distance of approximately 135 cm. Figure 3.3 is a plot of the average velocity of the gas in the direction of the flow against its distance down the geometry, information which will prove useful in calculating relaxation due to magnetic field inhomogeneities. The fuzzy region in both plots is due to the error in calculating pressures in the intermediate flow regime that was described above. Section 3.2.3 gives a description of how this particular distance scale came to be used.

Recalling that the cell must be run at approximately 15 atmospheres, we are dismayed to discover that the pressure at the end of the capillary tube is only on the
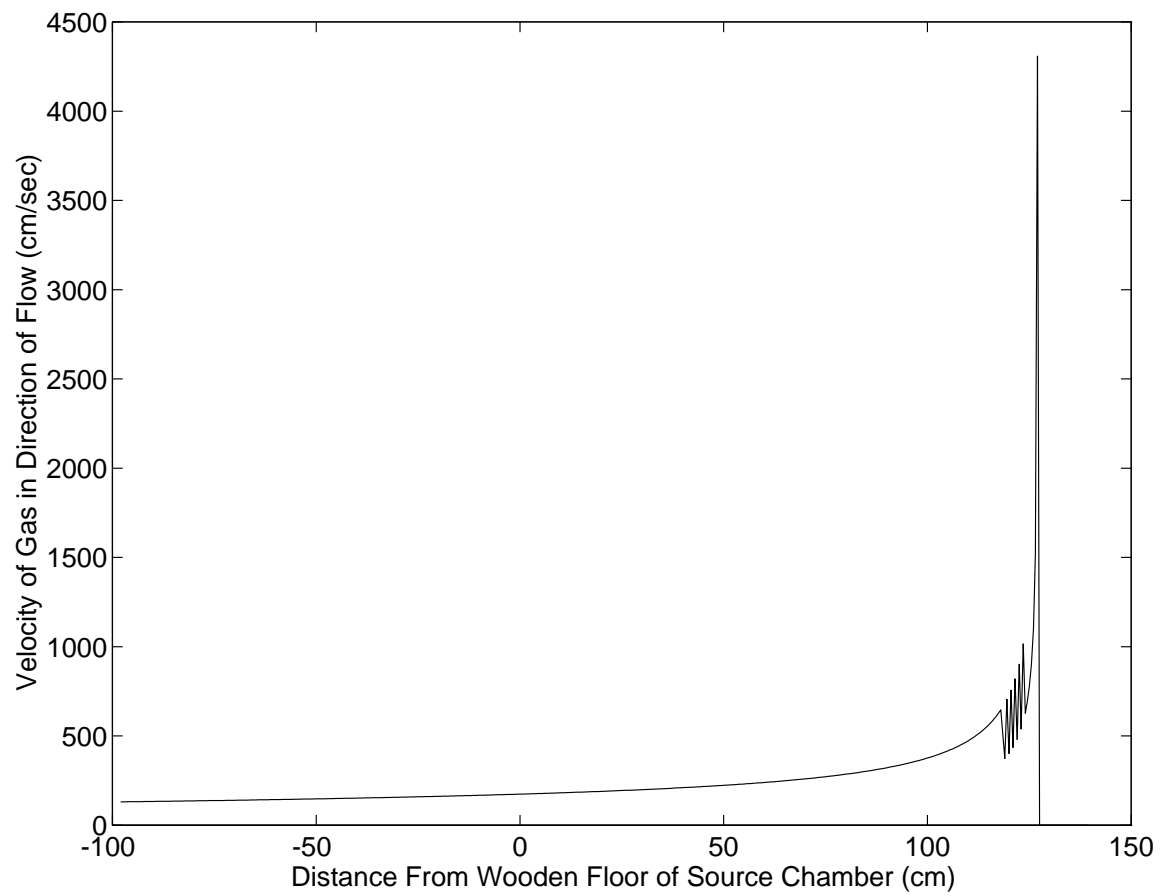
Figure 3.3: Plot of Velocity of Gas in the Direction of Flow versus Distance from Wood Floor of Source Chamber.

order of several hundred torr. The nature of the obstacle is now fully elucidated. We must somehow make the transition from a few hundred torr to 15 atmospheres within the very small distance separating the capillary tube from the cell. Accomplishing this feat took hours of calculation and days on the phone with salespeople.

3.1.2 Flow through a Really, Really Small Hole

The first idea for a solution of this problem might be to simply lengthen the capillary. However, it would take many meters of capillary .01 inches in diameter to achieve the desired pressure drop. The next idea is perhaps to make the inner diameter of the capillary smaller. However, capillary with an inner diameter of .01 inches is hard enough to obtain, especially when we want the metal to be non-magnetic. Extensive calculation showed that a minimum two order of magnitude decrease in the inner diameter of the capillary would be necessary to even approach the pressure drop needed, and lengths of tube with this diameter are not readily available, as many amused salespeople were quick to point out.

Discounting the alteration of the capillary tube, another early idea was to have some sort of regulation device between the cell and the tube. This device would either keep a constant pressure at the top of the tube, or maintain a constant mass flow rate throughout the system. After examining this possibility, we concluded two things. One, using such a device is not a viable option. All of the pressure and mass flow control devices that were examined had one or more of the following fatal flaws: they were extremely expensive, they contained a solenoid or other electronic equipment, or they were not bakeable to high temperature, eliminating the possibility of the sort of purity enhancing bakeout that will be described later. An adjustable leak valve seemed to be the most promising candidate, but we could not specify the material out

of which the inside of the valve was made, and so had no way of knowing how much this valve would affect the polarization of the gas. The second thing we concluded after a great deal of investigation into the matter was that we could not go with the earlier idea of having a set volume of gas that would then be polarized. This can be seen by looking at the time scale of a possible run with the polarized ^{3}He beam. Ideally, the possibility of running for many hours, if not days, should be kept open. It is not presently possible to build a cell containing enough gas to accomplish this, nor is it feasible to switch cells during operation, as this would be both difficult from a practical standpoint, and undesirable due to the probability of introducing impurities into the system during the switch. Furthermore, the pressure in a given cell declines as it is used, and, even with some way to keep a constant pressure in the capillary tube, a great deal of highly expensive gas will be wasted in each cell. Thus, we decided to build a flowing system. Due to the slow flow rate of the gas out of the cell, the average gas molecule spends over ten hours in the $\sim$ 300 cc cell, which should be more than enough time to achieve a high degree of polarization. The flowing system is therefore a viable alternative. The basic design of this system is described in section 3.2.2, and its implementation is detailed in chapter five.

So, we are left with very few possibilities. It seems that we must utilize the dynamics of gas flow in order to achieve this pressure drop, as mechanical help is not available, but no obtainable configuration of capillary tubing seems to work. Fortunately, this obstacle can be overcome. Although capillary tubing of sufficiently small diameter is not available, there are other usable geometries besides tubing. Most notably, as we can see from (3.11), if an aperture with a diameter on the order of a few microns could be found, this aperture would, theoretically, yield the correct flow rate. Finding someone to make such an aperture was no small feat, but, after amusing many more salespeople, we came upon the company Lenox Laser, which, if for no

other reason, should be mentioned here because of their telephone number: 800-49-HOLES. Using the technique of laser drilling, this company can make extremely small holes in gaskets made from stainless steel or copper. A full account of the testing and eventual verification of the usability of these holes can be found in chapter four, but it suffices to say here that these holes appear to work. As an added bonus, Lenox Laser has the capability of gold-plating these apertures, hopefully reducing wall relaxation due to collisions of gas molecules with the material from which the aperture is made. Two sample apertures, as seen through a microscope, are shown in figure 3.4.

3.2 Polarization Loss

Now that we have designed a workable geometry of the gas flow system, and have determined the pressure at each point in this geometry, we can begin to characterize the loss in polarization that the gas experiences in its travel through the system. As mentioned above, while there are many causes of depolarization over which we have no control, there are some that we can minimize. The three most apparent alterable determinants of depolarization are: interactions with the walls of the tubes, gaseous impurities, and relaxation due to magnetic field inhomogeneities.

3.2.1 Wall Relaxation

The easiest of these three factors to minimize is depolarization due to interactions with the walls. The steps taken to minimize relaxation with the cell walls have been described above, and the aperture was gold plated to prevent relaxation due to interactions with it. This leaves two main parts of the apparatus as yet unaccounted for: the tubes and the connections. By choosing non-magnetic materials for the tubes, we hope to limit the degree of relaxation caused by them. Originally, we intended
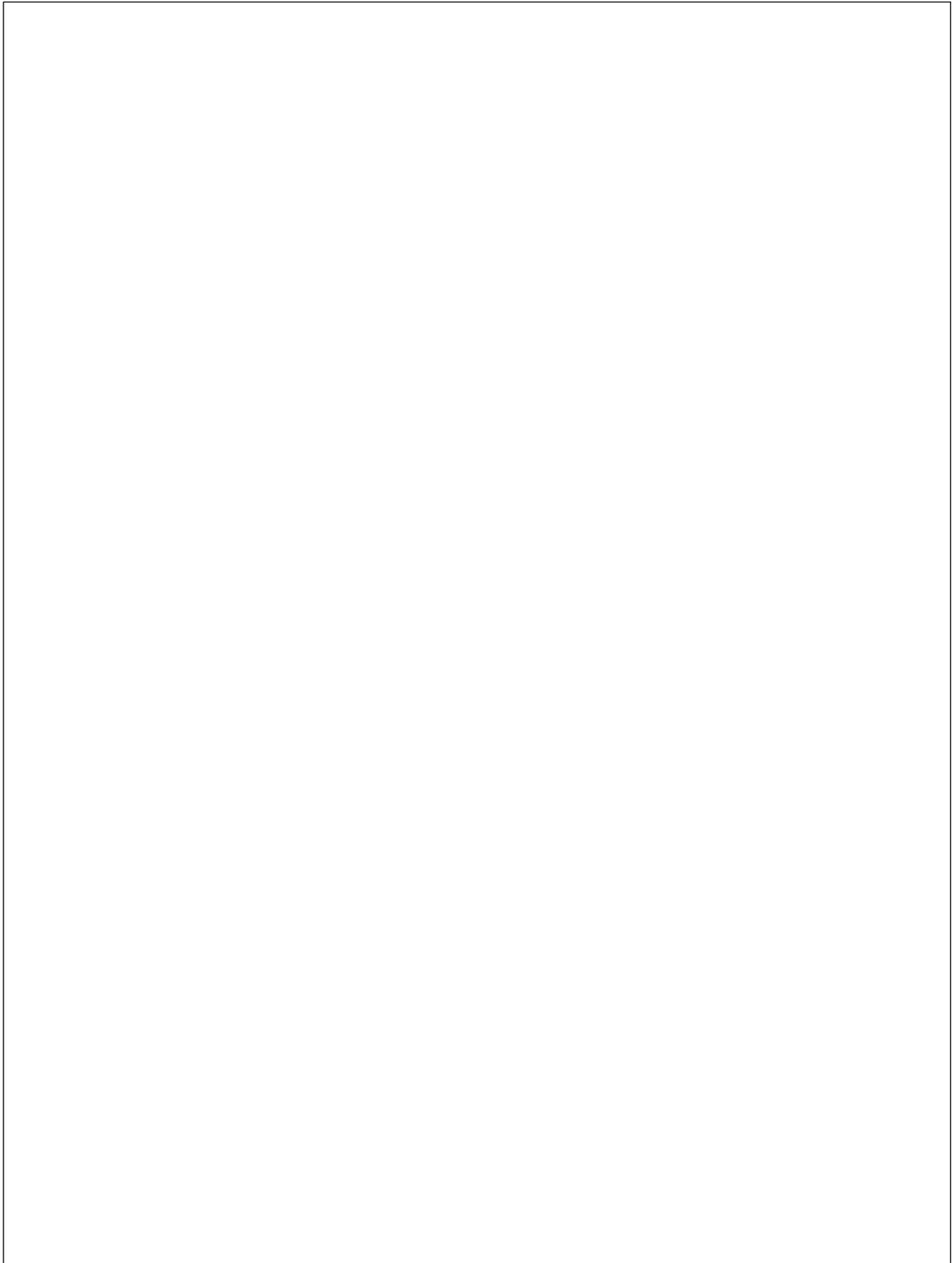
Figure 3.4: 1.5 and 2 Micron Apertures as Seen under Microscope, with Scales

to use pyrex or aluminosilicate glass as much as possible in the tubing, with gold or platinum to be used in the fixed length, since glass is not an option there. However, this idea proved impractical. Glass is too rigid and too fragile to be convenient to use as a link between the cell and the fixed length, taking into consideration that the cell will likely be some distance from the cyclotron source, given the small size of the chamber in which the source is located. While gold tubing of sufficiently small inner diameter was available, its high price and lack of mechanical strength made its use questionable. After discarding these options, we decided to go with copper tubing for the fixed length. Copper tubing is available with the required inner diameter, and the cost of this tubing is substantially less than that of the gold tubing. Furthermore, we do not expect wall interactions to be a significant factor in relaxing the gas during its passage through the fixed length. By the conservation of energy, gas molecules that move to a lower pressure from a higher pressure must increase in speed, and so, by the time it reaches the fixed length, the gas will be moving very fast indeed. In fact, the average gas molecule will likely spend only a fraction of a section in the entire fixed length, and we do not expect much of an effect from the walls of the copper tube on this timescale. Additionally, because of the short amount of time the gas spends even in the capillary tubing, we have decided to do the most convenient thing and simply use the same diameter copper tubing for the capillary as well. Embedding these tubes within larger diameter stainless steel sheaths allows for a fairly easy installation into the source, and these sheaths also provide improved mechanical strength for the tubing.

Having specified the material from which the tubes are to be made, it remains to provide the details of the connections. Attached to the pumping cell via the output port is a glass-to-metal seal. The metal part of this seal is made from stainless steel, and, in order to prevent depolarization due to this metal, we had it gold-plated.

The glass to metal seal is connected to the stainless steel sheathed copper tube by high vacuum UltraTorr$^{\mathrm{TM}}$ connections. The form of these connections allows the two tubes that they join to press up against each other, minimizing dead space between the tubes in which the gas could depolarize. In addition to their effectiveness in reducing depolarization, these fittings are easy to use, making the connection between the tube that will be threaded through the gas intake line in the source and the capillary tube an easy one to make. This ease of use allows for a quick separation of these two sections, which makes the removal of the source for servicing a readily available option. After these lengths of copper tubing, no more connections are needed, since the gas exits from the fixed length directly into the ionization chamber, where it is hopefully ionized without a significant polarization loss, and then is sent into the cyclotron.

3.2.2 Gaseous Impurities

Relaxation due to gaseous impurities is somewhat harder to control, since it is virtually impossible to remove every single source of foreign substances that may be present within the gas handling system. Due to the choice of using pre-mixed gas, we were only able to obtain gas that is 99.995% pure, as opposed to the 99.9999% pure research grade gas that is possible. This source of impurities will be overshadowed, however, by the action of the rest of the gas handling system.

In order to maintain a pressure of 15 atmospheres in the pumping cell, the system must contain two essential pieces of equipment: a regulator and a pressure transducer. The regulator is necessary in order to move from the ~100 atmospheres of gas in the bottle to the 15 atmospheres in the rest of the system, and the transducer is required as a check of the regulator's accuracy, since a mistake in the pressure of the

pumping cell could lead to a very loud, very dangerous, and very costly explosion. Unfortunately, the vast majority of regulators and transducers are not instruments of high purity. Even those that are designated for use in high purity systems frequently do not display the attributes that we desire for our use. For instance, in order to increase the purity of the system we would want to be able to run a hot gas purge, using either argon or helium heated to 150 °C to outgas impurities from the tubes and to drive out foreign subtances such as water, which can be disasterous to polarization accumulation. However, most of these devices contain either sensitive electronics that cannot be heated, or, more frequently, parts made from plastics that melt at high temperatures. As the ability to run a hot purge is extremely desirable in our system, a great deal of time went into finding components that are both designated as high purity, an attribution which can be verified by examining their leak rate and inquiring as to the method of their purification, and able to take high temperatures during operation. While we were not completely successful in this endeavor, we did manage to find a high-purity stainless steel regulator that can be operated at slightly over 100 °C, and a flow-through pressure transducer that works at up to 125 °C. The fact that the pressure transducer is flow-through helps to reduce dead space that could collect impurities and be difficult to purge, and the transducer further justifies its high-purity designation by arriving fully cleaned and sealed in an argon bag.

Having acquired the regulator and the pressure transducer, we still needed a way to verify the flow rate. Finding such a device was difficult, given the dual constraints of an extremely low flow rate and high temperature operation. However, after a great deal of searching, a few such devices were found. While many were either too expensive or of dubious accuracy, a couple of workable models were found. We finally settled on a Hastings-Teledyne flow meter, which is able to operate at up to 200 °C. An MKS mass flow controller also fit the bill, and would additionally allow the flow

rate to be regulated, but we decided against it due to its high price and the fact that we already had a crude way to regulate the flow by using the regulator on the gas bottle. The only problem with the mass flow meter that we have chosen lies in its connection to the system. It has female NPT input and output ports, which is not an ideal situation. Unlike the VCR and UltraTorr$^{\text{TM}}$ connections that are present everwhere else in the system, except in the connection to the gas bottle, NPT is generally not considered a high-vacuum connection. Wrapping the connection with Teflon tape helps somewhat, but having a VCR connection welded to the flow meter would be a more desirable solution, and is definitely a possibility that needs to be examined in the future. In order to minimize any relaxing effect due to the meter, we have utilized a bypass around the flow meter. This allows us to remove the meter from the system so that we may check on the actual effect that it has on the polarization, and also to use a higher flow rate of purge gas without overloading the meter, which is designed for measuring rates between zero and ten sccm.

The purge is accomplished through the installation of a purge port between the regulator and the gas bottle, an output port before the cell, and a diaphragm pump which can be connected to the output port. Helium gas heated to approximately 100 °C is sent into the purge port, and then travels throughout the region before the pumping cell. After some time, the valve to the output port is closed, the pump is connected, and the region is pumped out. Although the diaphragm pump only yields a vacuum on the order of a torr, we have chosen to use it since it pollutes the system minimally. The area after the cell is continually pumped out to a pressure on the order of 0.1 Torr by by the pump connected to the cyclotron. This area can also be purged with the heated helium by closing off the output port and opening the valves leading into and out of the cell, but this should only be done when the region around the cell is sufficiently clean. Furthermore, the valve leading out of the cell should only

be opened after the chamber is at well over an atmosphere to prevent diffusion out of the cell.

In addition to all that is described above, two final things have been done to reduce the presence of gaseous impurities in the system. Every piece of stainless steel tubing before the pumping chamber was cleaned by ultrasounding them twice using acetone, and then once more using ethanol, and all connecting pieces save those on the devices described above have been scrubbed with acetone and ethanol applied to cotton swabs. We rely on the purge and the pump to clean the area after the cell. Finally, just to make sure that we have eliminated all possible impurities other than N_2 and ^{3}He , a nitrogen purifier made by UltraPure^{TM} is placed in the system directly before the output port. This purifier should theoretically remove everything from the gas mixture other than nitrogen and noble gases, thereby making many of the aforementioned precautions unnecessary. However, as no device is perfect, we have gone to great lengths to insure purity in our system so that, even if the purifier does not do its job perfectly, any polarization loss that we experience should not be a result of gaseous impurities. The complete gas handling system, up to the pumping chamber and inlcuding all of the pieces mentioned in this section, is diagrammed in figure 3.5.

3.2.3 Magnetic Field Inhomogeneities

Magnetic field inhomogeneities promise to be the most important of all causes of depolarization during the transport of ^{3}He into the cyclotron. Although there does exist a static magnetic field in the z-direction, in travelling through the capillary and the source tubing, while also undergoing motion due to thermal effects, the polarized spins of the ^{3}He nuclei sample many different variations of the magnetic field, and
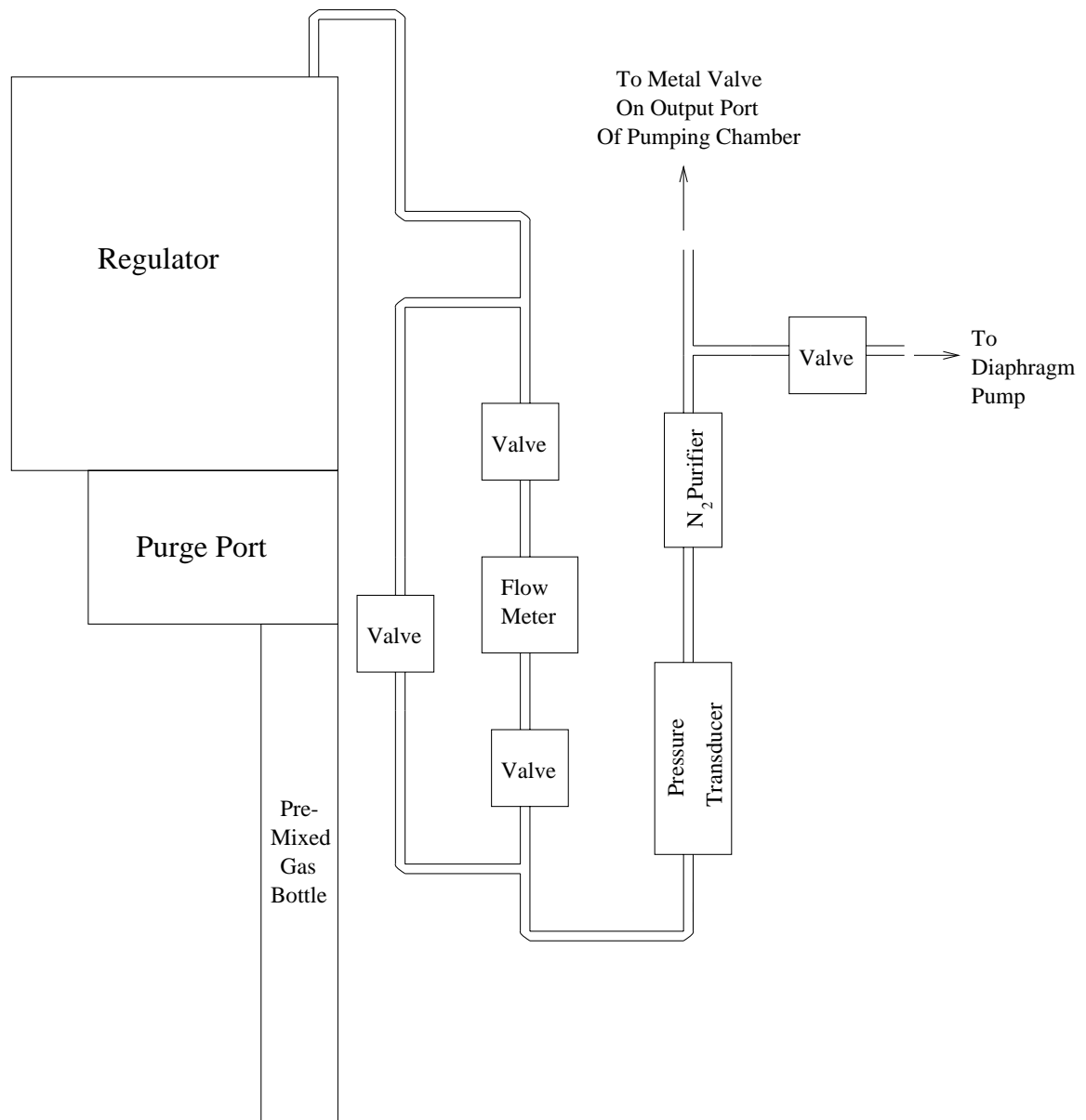
Figure 3.5: Scale Diagram of Gas Handling System up to the Pumping Chamber.

thus experience a time-varying component of the field in a direction perpendicular to it. This component causes the spin to precess around the new total magnetic field that is formed by the sum of the static and the time-varying components of the field. When the gas collides with either the walls of the tube or with other gas molecules, the time-varying component of the field suddenly changes in direction, resulting in the spin precessing around a different total field formed from the new sum. Successive collisions cause a net relaxation in the polarization of the gas [10, 16]. In the pumping chamber, this, along with other forms of relaxation, cause a lower maximum obtainable polarization, while, in the tubing through which the gas flows, this relaxation causes a decrease in the total amount of transferrable polarization.

A full derivation of the relaxation time attributed to magnetic field inhomogeneities using semi-classical methods can be found in [10], and one using quantum mechanical methods can be found in [16]. Since both agree to within a factor of $\sqrt{2}$, we will choose the result from Gamblin and Carver, which is derived in a more intuitive manner.

Each collision that the gas molecules undergo changes the direction of the time-varying component of the magnetic field in a fundamentally random manner. This change induces a displacement in the orientation of the spins with respect to the static magnetic field, which is found to be [10, eq. 18]

$$\Delta z = \sqrt{2} r (1 - \cos \omega \tau_c)^{\frac{1}{2}}, \tag{3.12}$$

where $\tau_c = \lambda / v_{av}$ is the gas correlation time, $\omega = \gamma B_0$ is the precessional frequency, and $r = \frac{B_{EFF}}{B_0}$. For small angles, r thus represents the angle between the static magnetic field and the inhomogenous component. Using the idea of the random walk, we can sum the average angular deviation of the spins from the static field after

n collisions, where n is some arbitrary number. This sum turns out to be [10, eq. 29]

$$\theta = \sqrt{n} \langle \Delta z^2 \rangle_{av}^{\frac{1}{2}}. \tag{3.13}$$

Seeking to find a characteristic relaxation time, we specify n to be the average number of collisions which yield a polarization loss of approxiamtely 63%, or $\frac{1}{e}$ times the original polarization. This n is [10, eq. 30]

$$n = \frac{1.42}{\langle \Delta z^2 \rangle_{av}}, \tag{3.14}$$

and now all that remains is to calculate $\langle \Delta z^2 \rangle_{av}$. With the rate of angular change in the total magnetic field being [10, eq. 33]

$$\frac{d\theta^2}{dt} = \frac{\left(\vec{\nabla} B_x \cdot \vec{v}\right)^2 + \left(\vec{\nabla} B_y \cdot \vec{v}\right)^2}{B_0^2}, \tag{3.15}$$

we average (3.15) over all directions of $\vec{v}$ and move to a frame rotating with the total magnetic field to yield [10, eq. 35]

$$B_{EFF} = \frac{\left\langle \frac{d\theta^2}{dt} \right\rangle_{av}^{\frac{1}{2}}}{\gamma B_{TOT}} = \left(\frac{v\delta B_{TOT}}{\gamma B_{TOT}}\right). \tag{3.16}$$

Integrating over the probability distribution of mean free paths gives the result [10, eq. 36]

$$\langle \Delta z^2 \rangle_{av} = \frac{\left(\frac{v\delta B_{TOT}}{\gamma B_{TOT}}\right)^2 2\omega^2 \tau_c^2}{\left(1 + \omega^2 \tau_c^2\right)}, \tag{3.17}$$

which, when coupled with (3.16), results in the following longitudinal spin relaxation rate [10, eq. 37]

$$\frac{1}{T_1} = \frac{\lambda v_{av}}{2.13(1 + \omega^2 \tau_c^2)} \frac{|\vec{\nabla} B_x|^2 + |\vec{\nabla} B_y|^2}{B_0^2}. \tag{3.18}$$

In order to minimize this rate, we must first be able to compute it for the situation at hand. This requries knowledge of both the static magnetic field and the magnetic field gradients in the perpendiular directions, as well as the mean free path, λ. Once

we have the tools necessary to accomplish this, we will integrate (3.18) from the time the gas enters the tube until the time it is injected into the ionization chamber. Making a determination of the time the gas spends at each point, as well as calculating the mean free path, requires knowledge of the pressure, the temperature, and the inner diameter of the tube through which the He^3 must travel.

The first step in this calculation was the measurement of the static magnetic field in a region ranging from slightly above the ion source to the area between the cyclotron dees. In order to find the magnetic field inside of the source, a field guide was inserted into the opening in which the source usually sits. The distance down into the guide was measured from a reference point above the source, a technique which was made fairly accurate by affixing the axial probe of the gaussmeter to a rigid metal rod. In transferring the data to disk for use in the previously described computer program, this reference point was changed to correspond to the wood floor of the ion source chamber, which, since it is a fixed point, makes the measurement theoretically repeatable. Negative distances correspond to regions above the floor, and positive values signify regions below the wood floor and, therefore, into the source. The data over the entire area of measurement, which wer taken at intervals of either 0.5 or 1 cm, depending upon the size of the gradient in that area, are plotted in figure 3.6. As we can see from the plot, the magnetic field in the z-direction varies relatively little up to a certain point, where it suddenly ramps up to a value of about 11 kG. Figure 3.7 is an enlargement of the graph showing those points leading up to this sharp increase, and it allows us to see that there are zeros in the magnetic field at two different points within the source. These zeros probably result from the interaction of the strong magnetic field from the cyclotron's magnet with the ferromagnetic iron that unfortunately surrounds the pit into which the source is lowered while running. The presence of these null field points means that, in order to prevent massive depolarization, an
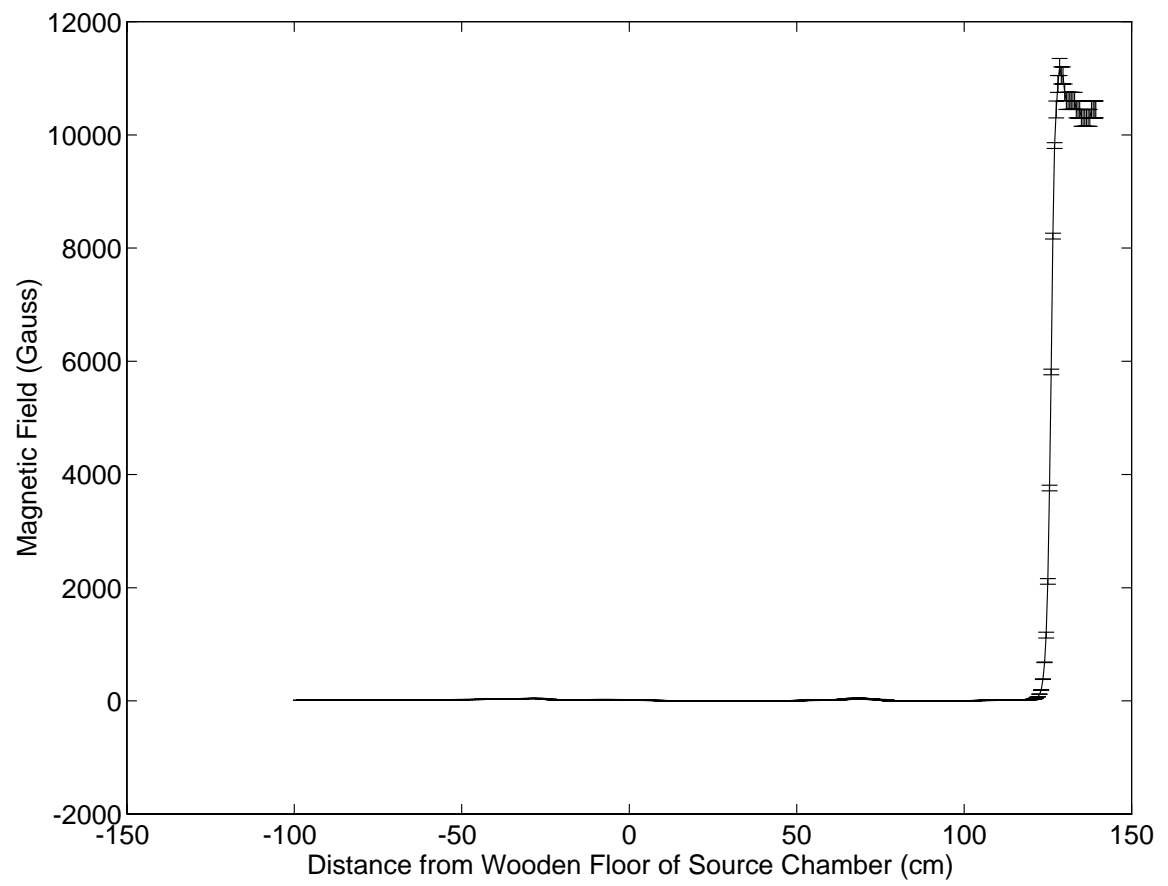
Figure 3.6: Plot of Magnetic Field in Source Chamber against Distance from Wood Floor.

external field must be added at these points. It is not difficult to construct a solenoid that can provide this field in the region of the first null point ranging from 21 to 32 cm, but, because of the form of the source, the use of a solenoid in the second region, ranging from 80 to 85 cm, is not so easily accomplished. While this problem is by no means insolvable, serious thought must be given to how this can be done. Given the form of (3.18), it is likely that we will want to add a static magnetic field at every point in the tube in order to minimize the relaxation rate. Thus, expanding the source pit to make room for the installation of a semi-permanent coil seems a possible option. Although we did not measure the transverse magnetic fields within the chamber directly, we can deduce the magnetic field gradients in these directions using our measurement of the field in the axial direction. The axial field gradient is first approximated by dividing the difference in field strength between two points by the distance separating these points. The computer program calculates this gradient using points at intervals of 0.5 cm, with the gradients at the first and the last points defined to be the same as the gradients at the next nearest points. The axial field gradient so generated is related to the transverse field gradients by the expression [6]

$$\vec{\nabla} B_x = \vec{\nabla} B_y = -\frac{1}{2}\vec{\nabla} B_0, \tag{3.19}$$

which is true for our case if we make the approximation of field cancellation in the transverse directions due to the symmetry of the cyclotron's magnetic field. Assuming this symmetric characterization is accurate, we have that

$$B_x = B_y = 0, \tag{3.20}$$

with

$$\frac{\partial B_x}{\partial x} = \frac{\partial B_y}{\partial y}, \tag{3.21}$$

and all of the rest of the partial derviatives, except for $\frac{\partial B_z}{\partial z}$, equal to zero. The non-existence of the magnetic monopole gives us the condition $\vec{\nabla} \cdot \vec{B} = \vec{0}$ which, when
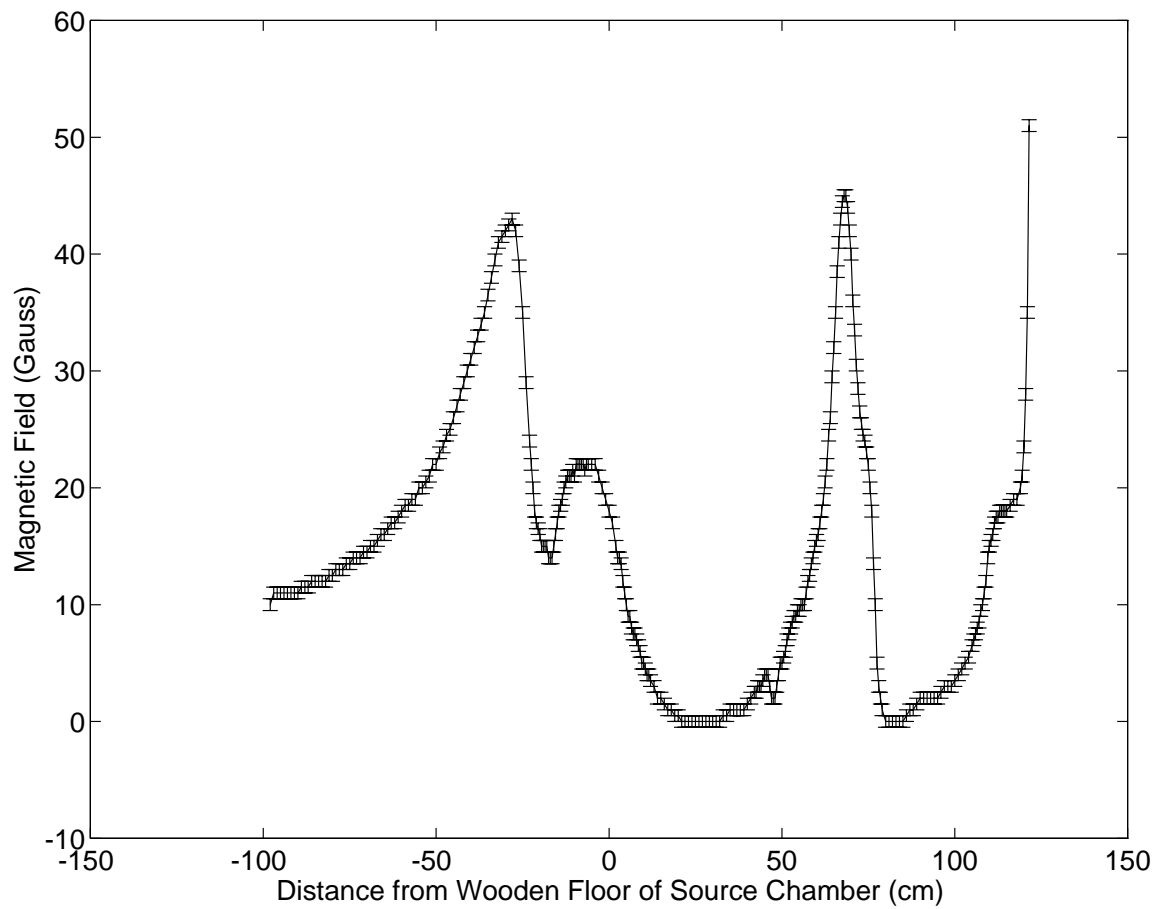
Figure 3.7: Blow-up of Magnetic Field Plot Highlighting zeroes in Field.

combined with (3.20), yields the previously stated result, (3.19). Of course perfect symmetry does not truly hold in our situation but, as in most areas of physics, the approximation will be good enough.

With this magnetic field information in hand, we can now utilize our knowledge of the pressure at each point in the system. The program, which now stores data for the magnetic field, transverse field gradients, and pressure at every point in the system, uses these values to compute (3.18) at each one of these points. The mean free path is calculated by combining the pressure with (3.3) and then comparing this result to the radius of the tube at the point in question. The smaller of these two values is then taken to be the effective mean free path. The average velocity of the gas molecules is obtained by assuming that the velocities follow a Maxwellian distribution, and is [14, eq. 2.42]

$$v_{av} = 1.45 \times 10^4 (T/M)^{\frac{1}{2}} \quad \frac{\text{cm}}{\text{sec}}. \tag{3.22}$$

Taking the gyromagnetic ratio of ^{3}He to be -2.0348$\times 10^4$ $\frac{\text{rad}}{\text{sec·gauss}}$, which was obtained by scaling from the value of the gyromagnetic ratio of the proton, and using the geometry of the system that was described above, the program combines the magnetic field data with the room temperature gas flow data to determine the value of the relaxation rate, given by (3.18), at every point.

Once it has determined $\frac{1}{T_1}$ throughout the system, the program proceeds to integrate this rate over the time that an average gas molecule spends in the system in order to determine the total loss in polarization that the gas is likely to experience during transport into the cyclotron. The interval of integration is taken to be 0.5 cm, which is the minimum distance for which data points are available. This distance is converted to a time, which is more useful in the integration, by using the throughput of the gas. Dividing the throughput by the pressure difference between two points,

we obtain the volumetric flow rate between these points. From this result the area of the tube is divided out, giving the net speed at which gas molecules are flowing through the system. This velocity was plotted as a function of distance in figure 3.5 and, when divided into the standard 0.5 cm interval of distance, yields the average time it takes for the gas to traverse this interval. The program calculates these times, multiplies them by the corresponding relaxation rates, and sums the series to yield the total loss of polarization experienced by the gas in traveling into the cyclotron.

In the early stages of determining the feasibility of the experiment, several days were spent running the program with varying temperatures, inner diameters of both tubes, and added magnetic fields. Including the mandatory added magnetic field, which, for simplicity, we took to be 10 gauss, we found an 87.58% polarization loss using the present configuration of the source, which contains a gas delivery tube that has an inner diameter of $\frac{1}{16}$ of an inch. This is clearly unacceptable. However, in examining the data obtained by cycling through different values of the variables, we found that losses as low as a few percent could be obtained. Shrinking the inner diameter of the fixed length tube seemed to have the most effect on this, although lowering the temperature and raising the magnetic field also had substantial results. Discussions with Steve Kidner, who holds a wealth of knowledge about the Princeton cylcotron and whose help has been invaluable to this project, helped to clarify the the relative ease of putting into effect the available solutions. While it was possible to cool the gas travelling into the cyclotron, and obtain less of a loss in that manner, this cooling could not be easily done, especially not without seriously altering the source, something that we were attempting to avoid. As we pointed out earlier, an additional magnetic field must be added to prevent a catastrophe, but it is difficult to obtain much more than the ten gauss that we are assuming, and this small field is not enough to lower the polarization loss to the degree at which we would like to

see it. Changing the inner diameter of both tubes, however, is not an impossibile job. Steve was able to thread the stainless steel sheathed copper tube through the gas delivery line, thus enabling a relatively easy installation. Although the effect of the capillary tube diameter upon relaxation is much less than that of the fixed tube diameter, due to the fact that the magnetic field gradients are much less in the region that the capillary tube occupies, we decided to go with the 0.01 inch inner diameter tubing for the capillary as well, as this would be the easiest tubing to connect to the source. With an added magnetic field of 10 gauss, an inner diameter of 0.01 inches, and everything at room temperature, we predict a total polarization loss of 3.6%, a great improvement over the previous result, and one which was accomplished with basically little alteration of the source. Although this calculation assumes a capillary length of 138.5 cm, which is a good deal less than its likely length, this was done only to match the length of the tubes with the available data regarding the magnetic field and is not expected to change things to any great degree, considering the relative homogeneity of the field at the upper reaches of the capillary. This small polarization loss demonstrates the feasibility of this project. The tests described in the next two chapters help to verify these calculations, leaving the way open for a full implementation of the polarized ^{3}He beam and the eventual accomplishment of a ^{19}Ne experiment.

Chapter 4

Pressure and Flow Studies

Before attempting to polarize a quantity of ^{3}He , it is wise to make absolutely certain that we can send it through the gas handling system at the needed flow rate without any significant problems. This is especially true given the expensive nature of the gas mixture that we are using. Losing a few dollars worth of ^{4}He due to a leak in the tube connections or, more likely, a rupture in some vital part of the system, like the small aperture or the gas cells, is one thing; losing several thousand dollars worth of ^{3}He for the same reasons is quite something else. Tests of both the calculations described in the previous chapter and some of the vital apparatus necessary for the polarized gas delivery system are thus in order, and this chapter presents the results of these studies of pressure tolerance and flow rate.

4.1 Pressure Tests

The first step in constructing any high pressure device is to make sure that it can withstand high pressures. The high cost of the gas, coupled with the danger of explosion inherent to a glass cell under 15 atmospheres of pressure, makes such tests essential procedure. We therefore began by obtaining a mock-up of the glass cell that we wanted to use for a pumping chamber. This test cell is virtually identical to the

final cell, except that it is somewhat longer, being 12.7 cm is length rather than 12.0 cm, and that it lacks the two capillaries which extend from the pumping chamber. Although we understand that it is entirely possible that these capillaries could break on the system, this breakage would most likely be from external mechanical stress and strain, rather than from the effects of internal force due to pressure, given the small area of the capillaries. Thus, including the capillaries in the pressure test is not all that relevant.

The test was conducted by filling the cell with water, submerging it, and then attaching it to a water-filled tube connected to a regulator, which was in turn connected to a large helium bottle. The cell was then covered by a plastic bag and placed behind a blast shield. The hope was that the sum of these precautions might prevent injury in case of a rupture of the cell. Of course, hearing protection was used as well, since the explosion could have been quite loud. The cell was then taken to a pressure of 23 atmospheres, well above any pressure at which we would need to run it, and held there for fifteen minutes. At the conclusion of this time we found that the cell was still intact, a fact that led us to conclude that our pumping cell should be able to hold the 15 atmospheres of gas pressure at which we would want to run.

In addition to the cell, we also pressure tested the bellows leading into the pumping cell in a similar manner. The bellows was taken to approximately 20 atmospheres and held there for 15 minutes, after which time no leak was found. It should be noted that the test was conducted with the bellows encased in a wood support designed to limit the stress on the bellows, a practice which we will follow in the final configuration as well.

The final piece of equipment that we tested was the small aperture that is the center of the flow rate studies. In order to test this aperture, which is made in a VCR gasket, we used the gasket to join two VCR glands. One end of this seal was

connected via a tube to a regulator, and the other was connected to a long tube. We then pressurized the aperture to approximately 20 atmospheres for 15 minutes, noting the pressure change in the regulator during this time. Since the gas bottle was closed, any change in the pressure at the input side of the regulator had to have come from leakage through the hole. We found that this leak rate was approximately what we expected it to be given the diameter of the aperture, and so concluded that the hole neither shattered nor expanded appreciably under high pressures.

4.2 Flow Tests

4.2.1 Apparatus

Having made sure that the most delicate pieces of equipment that would be present in the final configuration could withstand the pressures required of them, we moved on to testing whether or not the calculations of flow rate were correct. This was a necessary step since it is not easy to change the aperture while the VCR connection is attached to the pumping cell via a glass-to-metal seal, as it is in the final configuration of the delivery system. Therefore, we wanted to make sure that we had the size of the aperture right the first time.

Since we simply desired to test the flow rate, and did not particularly care about the purity of the system, we were able to take many shortcuts in designing the test apparatus. The first of these simplifications was the use of ^{4}He rather than the expensive gas mixture. Although the flow rate is dependent upon the mass of the gas that is flowing, it was not difficult to make a temporary change in the program that accounts for this. Furthermore, many of the properties of ^{4}He and ^{3}He are similar, so it is not a bad approximation to assume that characteristics like the viscosity of the

gas stay the same in switching from ^{3}He to ^{4}He. We obtained a semi-pure regulator to connect to the gas bottle, and attached the regulator in turn to a $\frac{1}{4}$ inch inner diameter copper tube. This tube was originally planned to connect to a non-bakeable flow-meter, which would make reading off the flow rates that we achieved simple. However, the flow-meter that we bought for the job turned out to be extremely flaky, and so, after a few days of trying to work with it, we removed it from the system entirely. Without a flow-meter, the tube from the regulator formed the input to an MDC$^{\text{TM}}$ four-way cross. Of the three other ports on the cross, one was connected to a tube that could be used for pumping out the system, one was attached to a pressure transducer, and the third was connected to a valve, which in turn was attached to the aperture. Time and monetary constraits prevented us from obtaining a pressure transducer that measured pressures over 150 psig, but this proved to be sufficient for our purposes.

On the other end of the aperture, which was made in a VCR gasket and tightened between two VCR glands, was a thirteen foot long $\frac{1}{16}$ inch inner diameter stainless steel tube, which was an early choice for the diameter of the tube running between the pumping chamber and the fixed length. This tube was soft soldered to a 70 cm long 0.01 inch inner diameter stainless steel tube, which took the place of the tube in the fixed length. This thin tube was then connected to another four-way cross, which had one of the four ports sealed. The two remaining open ports were connected to a low-pressure pressure transducer, and another pump-out port. With this setup, which is graphically depicted in figure 4.1, we were able to test the accuracy of the flow calculations and the performance of the apertures by looking at the pressure drop in the first four-way cross over time. Since the volume of the cross is a known quantity, we estimated the volume of the tubes between the regulator and the aperture to yield a total volume of 254 cc. Multiplying the change in pressure over time by this
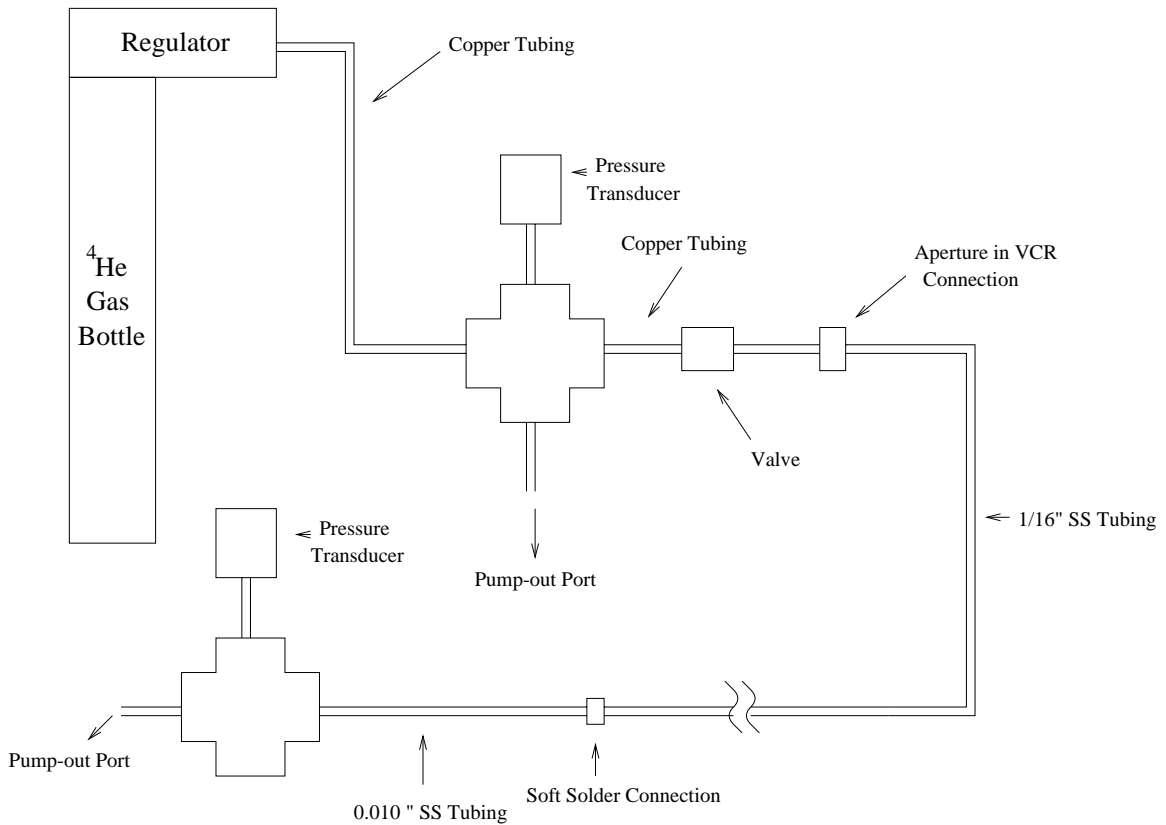
Figure 4.1: Diagram of the Flow Test System (Not to Scale)

constant volume, and then converting to the units of (std.) cc/min, we calculated the leak rate through the aperture in each case, which gave us a rough idea of the flow rate through the system. Unfortunately, the low pressure transducer measured only gauge pressure, so we were not able to get a measurement of the pressure in the downstream four-way cross. However, since the pressure upstream of the aperture is highly dependent on the diameter of the aperture, and as Lenox Laser can only supply apertures with gradations of 0.5 microns, the rough measure of the flow rate gained from examining the pressure change in the upstream four-way cross was sufficient for our purposes.

4.2.2 Results

For the first series of tests we obtained five 4 micron apertures, three of which were made from stainless steel, and two of which were made from copper. Using the program to calculate the pressure of ^{4}He necessary to yield a flow rate of 2 sccm, we found that we should pressurize the upstream four-way cross to 7.9 atmospheres. Doing this, we then watched the pressure drop in the upstream cross for a total of three minutes, with the first stainless steel hole in the VCR connection. This yielded a virtually constant pressure drop each minute, with the only change in the drop over time being a result of the steadily decreasing pressure upstream of the aperture. This constancy implied that the holes do not widen appreciably over time, a very favorable result. Unfortunately, the constant pressure drop was 55 Torr per minute, which equates to a flow rate of 18.47 sccm, which is very, very far from what we can use in the cyclotron. Checking for a leak elsewhere in the system, we closed the valve located right before the aperture and observed the pressure drop over an equal length of time. However, this leak rate was only 2.3 sccm, not nearly enough to account for the large discrepancy in the measured versus the calculated flow rate. Inputting a flow rate of 16.16 sccm into the program, and looking for a pressure of 7.9 atmospheres, we find that the hole would have to be aproximately 8.45 microns in diameter, instead of 4 microns, if the calculated and the experimental results were to be reconciled. Before testing this, however, we took the first stainless steel hole out of the VCR connection, and then replaced it again. While this proceedure is generally not recommended for high vacuum work, we felt that it would not matter greatly for our low vacuum application. Before testing the hole again, we also tightened all of the connections surrounding the hole, which proved to remove the small leak that we saw earlier. Measuring the pressure drop for this same hole, we found a leak rate

of 13.8 sccm, slightly better than the previous measurement, but still nowhere near satisfactory.

After this disappointment, we decided to take a look at the remaining apertures. The second stainless steel hole that we used yielded even worse results, showing a flow rate of 62.345 sccm. Again using the program to determine the requisite hole diameter at 7.9 atmospheres that would yield this flow rate, we find an aperture diameter of 13.85 microns. Moving to the copper holes in the hopes of finding better results, we were disappointed. The first copper hole yielded a flow rate of 111.61 sccm, which corresponds to a hole diameter of 17.3 microns. In addition, after removing the hole we found that the copper had significantly deformed under the pressure. The second copper hole was slightly better, but still not good, giving a flow rate of 48.49 sccm, which corresponds to a hole diameter of 12.55 microns. Unfortunately, after use we discovered that the hole had completely shattered, cracking along the circle at which it was deformed by the VCR glands. From this experience with the copper holes, we determined that we needed gaskets made from a stronger material in order to take the pressure. Since these apertures were only available in a narrow range of materials, we were forced to stay with stainless steel, which is what led in part to our present use of a gold-plated stainless steel gasket for the aperture.

In order to see which was at fault, our calculations or the aperture manufacturer, we looked at the second copper aperture under a high-powered microscope. Here we found some degree of solace, as, by comparing the aperture to a microscopic grating, we we able to determine that the aperture was aproximately 10 microns in diameter, a value that is fairly close to the 12.55 that the calculations predicted. In addition, the retest of the first hole hinted that the apertures tend to close up after use, due probably to the accumulation of tiny particles along the edges of the hole. Further experiments verified this fact. This might account for some of the remaining

discrepancy between the observed value of 10 microns, and the calculated value of 12.55 microns.

As the blame for the failure of the aperture apparently fell mostly on the manufacturer of the holes, we decided to try our luck again, and purchased two more stainless steel holes, this time with diameters of 1.5 and 2 microns. Tests for these holes proceeded far better than previously. The 1.5 micron hole appeared to be just as bad as the other holes at first look, but, after tightening, we achieved a flow rate of 0.308 sccm over the span of 15 minutes, at a pressure of 7.94 atmospheres. This corresponds to a hole diameter of 2.07 microns, very close to the 1.5 microns to which the hole is supposed to be laser drilled. The 2 micron hole yielded similarly encouraging results, with a flow rate of 0.462 sccm at 7.855 atmospheres. This corresponds to an aperture diameter of 2.38 microns, again very close to the value claimed by the manufacturer. Carefully removing this 2 micron hole after testing, and replacing it in its sealed case, we were able to repeat the measurement on this hole a full two weeks later, obtaining an identical result. Measuring the two holes under the microscope, we found that the diameter of each of the holes appeared to be approximately 2 microns, virtually matching our experimentally calculated result, especially given the possibility of a slight narrowing of the holes due to particular accumulation. It was these two holes that are displayed in figure 3.4.

The next step after these successful tests was to obtain apertures closer to the diameter that we would want to use. We therefore proceeded to order and test three more apertures, of diameters 3, 3.5, and 4 microns, hoping that these apertures would not have the same problems as the earlier 4 micron apertures. Upon first testing, we found some very disturbing results. The 3 micron hole yielded a flow rate of 0.924 sccm, which corresponds to a hole diameter of 3.05 microns, almost exactly on target. However, this result was not repeatable, and further measurements of this

hole yielded flow rates only half as large. A similar problem was found with the 4 micron hole. At first use it yielded a flow rate of 0.616 sccm, but upon retesting the flow rate had dropped to only 0.154 sccm. Both of these values were far less than expected. The 3.5 micron aperture had an even worse problem. First, measuring the flow rate through the hole, we obtained a leak rate of 1.847 sccm, greater than the 1.37 sccm that we expected at 7.9 atmospheres, but still within the realm of acceptability. However, subsequent measurements produced varying effects. The second time we measured the hole, after having removed and replaced it once, we found a flow rate of 3.69 sccm. Tightening the gasket within the VCR connection, we repeated the measurement. This time we obtained a flow rate of 0.77. Luckily, there was a solution to this problem. Remembering how the previous holes had narrowed over the time that they were removed from the connection, we proceeded to ultrasound the 3.5 micron aperture using both acetone and ethanol. Replacing the gasket in the VCR connection and making sure that it was well tightened, we measured the flow rate again and obtained a value of 1.847 sccm, exactly the same result that we obtained previously. A second measurement without altering anything yielded the identical result, and a third gave the flow rate 1.385 sccm, almost exactly what we had calculated for the 3.5 micron hole. However, this third measurement was also accompanied by a significant leak, so it should perhaps not be taken as seriously as the previous two measurements. Nevertheless, we have demonstrated that we can repeatedly attain a reasonable flow rate using the 3.5 micron hole, and that this flow rate is somewhere between 1.348 and 1.011 times the flow rate that we calculated. A summary of this data is shown in table 4.1.

We may use this information to settle on an aperture diameter for the final configuration. For a diameter of 3 microns, a calculation shows that a pressure of 25.1 atmospheres would be needed to attain a flow rate of 2 sccm, while for a diameter of

	Hole Size	Flow Rate	Actual Size	Expected Rate	
(1)	4 microns, SS #1	16.16 sccm	8.45 microns		
(2)	4 microns SS #1	13.8 sccm			
	4 microns SS #2	62.345 sccm	13.85 microns		Holes Were Too Big
	4 microns Cu #1	111.61 sccm	17.3 microns		
	4 microns Cu #2	48.49 sccm	12.55 microns		
	1.5 microns SS	0.308 sccm	2.07 microns		Holes Virtually Correct
	2 microns SS	0.462 sccm	2.38 microns		
	3 microns SS	0.924 sccm	3.05 microns		
(1)	4 microns SS #3	0.616 sccm			
(2)	4 microns SS #3	0.154 sccm			Flaky Holes
(1)	3.5 micron SS	1.847 sccm		1.37 sccm	
(2)	3.5 micron SS	3.69 sccm		1.37 sccm	
(3)	3.5 micron SS	0.77 sccm		1.37 sccm	
(4)	3.5 micron SS	1.847 sccm		1.37 sccm	Hole After Ultrasounding Is Much More Stable
(5)	3.5 micron SS	1.847 sccm		1.37 sccm	
(6)	3.5 micron SS	1.385 sccm		1.37 sccm	

Table 4.1: Summary of Flow Test Data. Numbers in Parentheses Signify Multiple Tests on the Same Hole.

3.5 microns we would need a pressure of 11.753 atmospheres to get the same flow rate. If we incorporate into the calculation the maximum 1.35 multiplier to the expected flow rate, we can obtain a range of possible pressures that might yield a flow rate of ~2 sccm. The pressure range for the 3 micron aperture was 14.92 - 25.1 atmospheres, and the pressure range for the 3.5 micron aperture was 7.02-11.753 atmospheres. This leaves us in a mild quandary, as the 3 micron aperture appears to be perfect if the maxiumum multiplier to the calculated value for the flow rate is used, whereas the 3.5 micron aperture seems to always yield a pressure that is too low for our use. However, there is also the question of safety. If the maximum multiplier turns out not to be applicable, then we will not be able to attain a flow rate of 2 sccm safely with the 3 micron hole. One fact can help us solve this dilemma, however. As a flow rate of 2.29 sccm is still acceptable for the cyclotron, we can let the flow be slightly higher without any significant negative impact. This flow rate, assuming no multiplier to our calculations, yields a pressure of 14.87 atmospheres using the 3.5 micron hole. This fact, coupled with the likelihood that we will want to run at lower pressures sometimes for safety reasons, leads to the conclusion that the 3.5 micron aperture is the best choice for use in the final configuration. In the next chapter, we will test this choice, along with the design of much of the gas delivery system, by attempting to look at polarization signals from a pressurized cell, and the amount of polarization loss after the gas has traveled through a mock-up system.

Chapter 5

Depolarization Studies

Having checked our flow calculations and settled on an aperture diameter, we may move on to the next test. Before making any alterations to the cyclotron, we should make sure that we can first polarize the relatively large volume of gas that will be present in the pumping chamber, and then transfer this polarized gas, without significant relaxation, down through both the aperture and a thin length of tubing. This procedure would allow us to isolate relaxation due to gaseous impurities and walls from relaxation due to magnetic field inhomogeneities, providing an independent test of the choice of components in the system and the sufficiency of the precautions taken to ensure the purity of the system. In order to accomplish these tests, we needed to build a workable system that is virtually identical in form to the final configuration that will be installed in the cyclotron.

5.1   The Apparatus

The fully implemented polarized gas delivery system consists of five basic parts: the pumping chamber, shown in figure 2.2, the gas handling system leading to the pumping chamber, diagrammed in figure 3.3, the tubing downstream of the pumping chamber, illustrated in figure 3.1, the diode laser array, and the oven that encompasses

the pumping chamber. If these five subsystems were to be connected and the tube threaded into the gas delivery line of the ion source, the apparatus for making the polarized ^{3}He beam a reality would be completed. However, in running this test outside the cyclotron, we need to include several other components. In order to measure the polarization coming out of the tube, as well as the polarization in the pumping chamber, three more pieces must be added. A second glass cell, similar but not identical to the first one, must be connected to the downstream end of the tube so that the polarized gas can collect in it and thus be studied. Measuring the polarization in both cells is challenging, especially considering the low pressure in the bottom cell. Finally, an applied magnetic field is necessary in order to provide a quantization axis for the spins, and to minimize relaxation due to magnetic field inhomogeneities. Furthermore, in order to apply the NMR techniques with which we want to measure the polarization, this applied field should be in excess of 20 Gauss. What follows is a description detailing the manner in which all of these components were obtained and the test apparatus was built.

5.1.1   Implementation of the Gas Delivery System Design

Much of the description of the gas delivery system is given in chapters 2 and 3, where all of the major design issues are laid out in detail. As these chapters also contain a recipe for the construction of this system, we will only describe here aspects of the system that have been changed for this test.

The pumping chamber was prepared in a manner identical to that described in section 2.2. The only thing to be noted in reference to the chamber is that these preparations took place over a week before the cell was filled for the first time with ^{3}He . During this time we noted a slight discoloration of the rubidium in the cell,

indicating the possibility of a tiny leak. However, as we leak tested the cell in the vacuum system before removing it and discovered no leak at the time, it is likely that any leak present was due to a slight loosening of the valves. Even though some of the rubidium was discolored, however, there still remained a substantial quantity unaffected, so the leak did not seem that serious, if there was one at all.

The gas handling system leading up to the cell was prepared in a manner nearly identical to that described in section 3.2.2. The non-magnetic stainless steel tubing was welded to the proper VCR connections by the shop, the necessary pieces were gold-plated, and all of the pieces were thoroughly cleaned before being connected, both through ultrasounding with acetone and ethanol, and hand cleaning using cotton swabs and the same two solvents. After its construction, the delivery system was attached to an aluminum frame which allowed easy access to all of the valves while providing sufficient suppport for the system.

The biggest change from the original design to this test occurred in the construction of the connection between the top and the bottom cells. We recall from chapters 3 and 4 that the design called for a 3.5 micron aperture in a gold plated stainless steel gasket, followed by a long copper tube of 0.01 inches inner diameter. However, due to an unforseen delay on the part of the manufacturer in gold plating the apertures, we were not able to receive gold plated apertures that we felt comfortable using in time for the test. Due to the time constraints of the thesis, we were forced to use a non-gold-plated 3.5 micron stainless steel gasket. Furthermore, we were not able to test the aperture beforehand, and did not clean the gasket in the manner described above. Although we do not expect the gas to relax much due to contact with the aperture, as the boundary layer of the gas against the gasket should be fairly immobile due to the high pressure upstream of the aperture, the use of this gasket is not ideal, and could cause some degree of depolarization. Besides the change of gasket,

we also altered the tubing running into the second cell in two ways. First of all, due to size constraints in the Helmholtz coils in which we placed the system, we used a 0.010 inch inner diameter copper tube that was only 36 inches long, the length of the fixed volume. Obviously, this reduces the amount of polarization loss that we see due to the tubing, since we simply have less tubing than will be present in the final configuration. Secondly, becuse we could not obtain a full complement of UltraTorr^{TM} connections, we were forced to use a combination of UltraTorr^{TM} and flex fittings. While the UltraTorr^{TM} fittings are high-vacuum, the flex fittings are not, a fact which could lead to the introduction of impurities into the system. It should also be noted that the tubing was not thoroughly cleaned, since we did not want to introduce acetone or ethanol into the system, as these chemicals might not evaporate fully due to the small diameter of the tube.

The inclusion of the diode laser array required little work on our part. Such an array had been in frequent use in experiments being conducted in both the atomic and the nuclear groups at Princeton University, and it was ready for our use when we wanted to run the tests. It simply needed to be aligned with the cell, and then was ready to run. Although precise statistics relating to the power dissipated in the cell were not available, we estimated that between 25 and 30 watts of the 50 watt laser that we ended up using in the test were centered on target.

The final component of the basic gas delivery system is the oven, which is used to reach the $\sim$ 180 °C temperature needed to obtain a sufficient number density of rubidium, as described in section 2.1. Again calling upon the resources of the atomic and nuclear groups, we were able to modify an oven that had been built for the SLAC experiments mentioned earlier. Made from high-temperature plastic, the oven body is able to withstand temperatures of up to $\sim$ 180 °C. It contains windows for the laser light to enter and exit the oven, and also has ports for the hot air intake and

exhaust, the input and output of the cell, and a viewport which is monitored by a camera for an easy check of the status of the cell. The temperature is controlled in the cell by a feedback mechanism, which alters the amount of heat transfered to the air that is constantly flowing around the cell. Holes at the bottom of the oven allowed us to mount it on the same aluminum frame to which the gas handling system was attached. The pumping chamber was then carefully placed into the oven, and a combination of insulation and high-temperature plastic supports was used to secure the cell in place. With this connection, the basic polarized gas delivery system was complete. We now move on to the subsidiary components.

5.1.2 The Second Cell

As stated above, we needed a second cell in order to provide for a volume that could hold the polarized gas that left the tube for measurement. The method of polarimetry that we used, as we shall see shortly, requires that, in order for the signals at both cells to be compared without significant additional error, the shape of both cells should be basically the same. A similarity in the cell design between the upstream and the downstream cell was also suggested by the fact that many of the same techniques used to limit depolarization were applicable in both cells. Thus, the second cell also was prepared on the vacuum system, although much less rubidium was deposited into it. We originally intended to use this rubidium as a getter to gather impurities to itself, but the rubidium in this cell showed the same signs of contamination as the pumping chamber did, and so it was not clear how effective this strategy turned out to be. The second cell had an input and a output port as well, and these ports were also made from 1 mm inner diameter glass capillary tubing to maximize diffusion times from the cell to the valves. The one difference between the first and the second cell

was the number of connections that we needed to make to each. While the first cell needed to be conected to both the gas handling system and the connective copper tubing, the second cell had different requirements. Measuring the polarimetry and the flow rate necessitated the presence of a pressure transducer at the bottom cell, and connections for the copper tubing and a pump out port for this tubing were needed as well. Thus, a total of three ports were required on the second cell. Putting this into effect made the second cell somewhat more fragile but, as the pressure in this cell is never supposed to reach an atmosphere, we were not overly worried. An illustration of the second cell, including all its ports and attachments, can be seen in figure 5.1.

5.1.3   Polarimetry

As mentioned above, resources from the atomic and nuclear groups at Princeton were essential in getting the tests up and running. Nowhere was this more evident than in regard to the polarimetry. Time constraints made it virtually impossible to design a polarimetry system for these tests; luckily, we did not even have to try. A great deal of work has been done by both Brian Saam, and recently by Christopher Erickson as well, in constructing a system of polarimetry based upon the ideas of pulse-NMR. We were very fortunate in having Brian Saam in the atomic group, as he not only let us borrow his pulse-NMR system, but took the polarization data for us as well. Since the extent of our work on the polarimetry system consisted only of constructing two surface coils for the cells, the polarimetry used in these tests will not be discussed in detail here. Instead, we will merely highlight the main points of the pulse-NMR method. A far fuller description of a system similar to the one we used can be found in the doctoral thesis of Brian Saam [15].
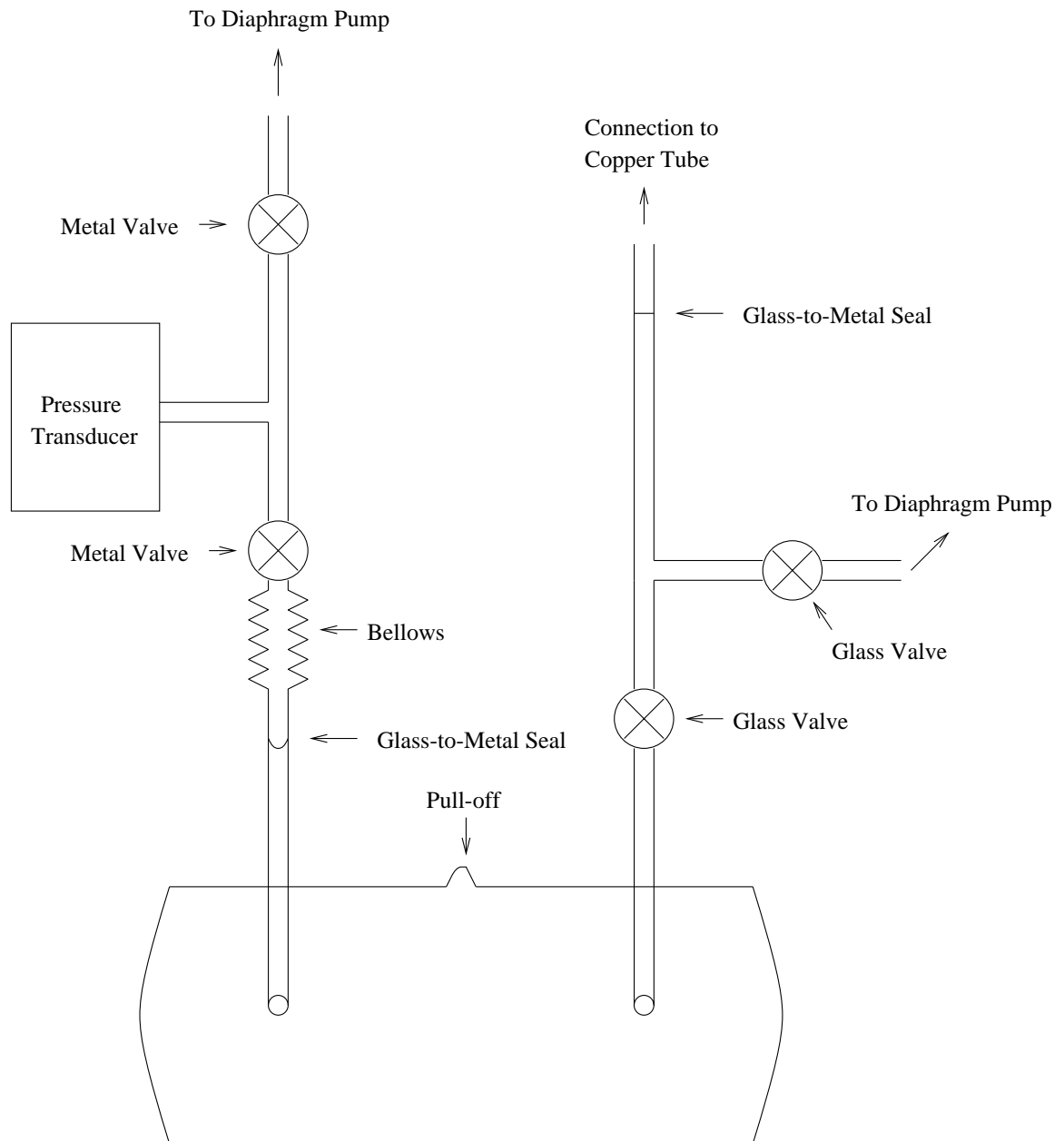
Figure 5.1: Diagram of the Second Cell, with Attachments

The basic idea behind pulse-NMR is fairly simple, although its application is far more complicated. Basically, we constructed two small coils of about an inch in outer diameter and $\frac{1}{2}$ inch in inner diameter, around which we wound aproximately 30 turns of copper wire to create an inductor with an inductance on the order of a milliHenry. These coils were then attached in parallel to both a BNC cable and a group of capacitors that are in series with each other, creating a probe which amplifies the signal that the coil receives. This probe is connected to a rack of electronics which can both generate RF pulses which are carried to the probe, and amplify and display return signals from the probe. These signals are saved by the oscilloscope, and later transferred to a computer for analysis.

The probes were attached to the top of each of the cells using Capton tape, and then connected to the rack of electronics. The coils were made from high-temperature plastic so that they could survive the heat in the oven. In operation, once there was thought to be a sufficient quantity of polarized gas in the cell, a pulse of RF was passed through the coil. This pulse in the coil creates a rotating magnetic field, causing the spins closest to the coil to precess around the static magnetic field at a tip angle dependent upon the strength of the applied RF pulse. In a system in which the whole cell is encased in a coil, the tip angle can be arbitrarily large, since all of the spins in the cell see basically the same rotating field. However, since we utilized a surface coil, the strength of the field was dependent upon the distance of the spins from the coil. In order to obtain an uniform measure of the polarization, therefore, the tip angle applied to the spins must be small, as a large tip angle could create a significant difference in the precession of the spins close to and far away from the coil.

After the pulse has been applied, the probe switches from being a transmitter of RF to being a signal receiver. The precessing spins induce an EMF in the coil according to Faraday's Law, $\mathcal{E} = -\frac{1}{c}\frac{d\Phi}{dt}$. This EMF is amplified and outputted to

the scope. Over time the freely precessing spins decay according to the characteristic transverse relaxation time, T_2^*. This decay is also recorded on the scope, and this form of measurement is known as looking at an FID, or free induction decay. The peak-to-peak height of the first peak shown on the scope gives the uncalibrated polarization of the sample in the cell. This uncalibrated signal is proportional to the product of the square of the gyromagnetic ratio of ^{3}He , the polarization of ^{3}He , and the number density of ^{3}He , which is dependent on the pressure of the ^{3}He in a given size cell. Calibration of this signal is usualy accomplished by comparison with the signal from a water cell. The polarization of a water sample in a low field is given by a Taylor expansion of the Boltzman distribution, and is $\frac{\mu B}{kT}$, where μ is the magnetic moment, B is the field, T is the temperature, and k is Boltzman's constant. Since the polarization, the gyromagnetic ratio, and the number density of water are all known, we can use the water signal to divide out the proportionality constant and determine the true polarization of the sample in the cell.

Since the pressure in the pumping chamber is very high, we expect that the signal generated from the polarized ^{3}He in the cell will be fairly easily seen over any noise that is present. However, the pressure in the second cell is very much lower, and so noise might play a significant role. To limit RF noise, the second cell was thus placed within an aluminum box, which was closed on four sides. This box was attached to the aforementioned aluminum frame, and the second cell was carefully supported inside the box by insulation and threaded brass rods. The pressure transducer connected to the output port of the cell was attached to the opposite end of the frame from the gas handling system, in order to provide further support for the apparatus.

5.1.4   Magnetic Field Coils and the Final Setup

With the addition of the pulse-NMR system, all that was needed for the final test was a large set of Helmholtz coils, capable of producing at least 20 Gauss. Drawing one more time upon the resources here at Princeton, we were able to borrow the roughly four foot diameter Helmholtz coils that had been recently used in tests of the aforementioned SLAC cells. As the entire gas delivery system was now attached to a single aluminum frame, we simply placed the frame in the middle of the coils attempting to center the cells in the coils as closely as possible. The coils were capable of producing a magnetic field of 40 gauss, which made them ideal for our purposes. In fact, we ran the experiment at a field of 38 gauss. Having placed the frame inside of the coils, made all of the necessary attachments, including connecting a bottle of 99.9999% pure helium to the purge port, and wrapped heater tape around the copper tube running from the purge port to the gas bottle in order to perform a hot purge, we were ready to begin the tests. A basic block diagram of the completed test steup is shown in figure 5.2.

5.2   Procedure and Results

The procedure that we followed in filling the pumping chamber, and then flowing the polarized ^{3}He through the aperture and the tube into the second cell, follows mostly from the discussion in section 3.2. We began by pumping out the system with the diaphragm pump. In the process of doing so, we found a significant leak, which had to be fixed by tightening the appropriate NPT connection before proceeding. After having reduced the leak to a minimal value, we completed the pump out to approximately 4 torr. We then proceeded to pump out the area around the pressure
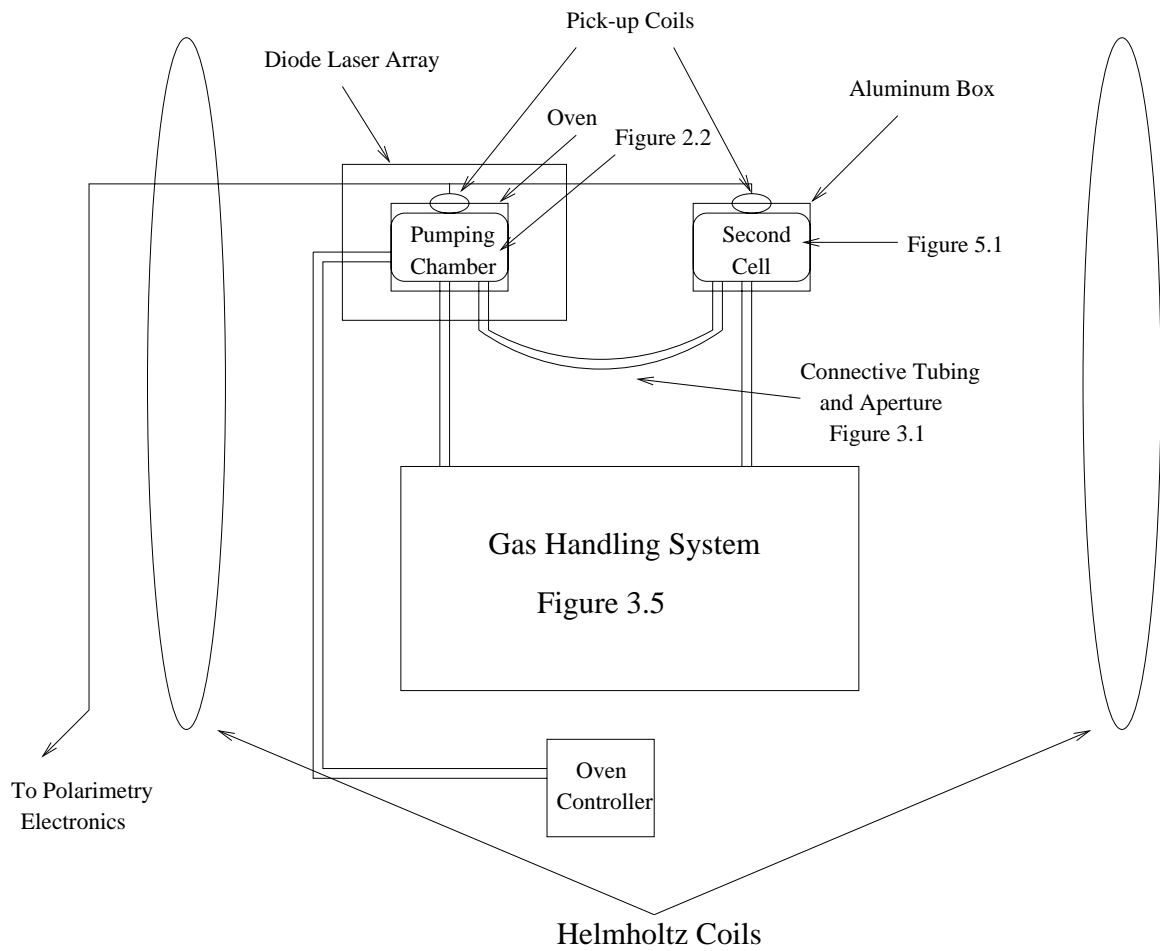
Figure 5.2: Block Diagram of the Setup for the Depolarization Tests

transducer that was located after the second cell. A hot purge was then completed on the gas handling system. After completing the purge, we again pumped out the gas handling system in preparation for the test.

The first part of the test centered on the pump-up of the cell. We began by beginning the heat-up of the cell, which was carefully monitored. The oven was eventually set to a temperature of 170 °C, although the temperature was up to 20 degrees higher inside the cell while running due to the heat generated by the laser. We then opened the valve to the cell and slowly filled it with the helium purge gas. Watching the pressure carefully, the cell was taken to a maximum pressure of 13.6 atmospheres at 170 °C. We waited for about an hour to make sure that the cell could withstand the pressure, and no problems manifested themselves during this time. The diode laser was then turned on, and this filling process was repeated using the premixed gas from the bottle. After attaining a pressure of 12.96 atmospheres in the heated cell, we closed the valves to the bottle and to the cell, and left the cell pumping overnight.

The pumping proceeded for about thirteen hours, during which time the pressure and temperature of the cell stayed roughly the same. After this time, the oven was turned down, and eventually off, so that measures of the polarization could be taken. A higher temperature would cause a change in the resistance of the copper wire in one of the pick-up coils, making it harder to relate the signals from the two coils accurately. The signal from the top cell was measured repeatedly over the next three hours or so. Although we did not get a water calibration due to problems with the NMR setup, and thus cannot give a value for the polarization in the top cell, we did see a very strong signal from this cell. Looking at the FID, we were able to extract a value for T_1, the inverse of the longitudinal relaxation rate, of 8.9 hours. This value compares favorably with the lifetimes of similar cells made in the group,

which generally range from 4 - 12 hours, with the occasional cell having a 20 hour lifetime. Cells in this lifetime range generally yielded polarizations in similar setups of about 10%, so it is likely that our polarization was somewhere near 10% as well. We consider this a success, as this is one of the first times a cell was filled outside of the vacuum system, and the first time that any cell was filled with this form of the gas handling system.

After this test, we pumped out both the second cell and the region between the two cells using the diaphragm pump. Completing this, we closed off the two pump ports, and opened the valve leading from the second cell to the capillary tubing. We then opened the output valve leading from the pumping chamber to the aperture, and watched as the pressure increased in the bottom cell. At this point in time, the top cell was at a pressure of 12.44 atmospheres, and we would expect from the flow rate calculations a leak rate through the aperture of 2.0672 sccm. Ordinarily we would simply measure the mass flow rate through the system with the mass flow meter. However, technical problems prevented the use of this meter. However, since we know that the volume of the bottom cell is ~ 285 cc, we can use the same trick of watching the pressure change in the cell that we used in our earlier flow studies in order to compute the flow rate through the system. We observed an average pressure rise of 5.687 torr in the bottom cell, which corresponds to a flow rate of 2.133, only a factor of 1.03 greater than the flow rate predicted by the calculations. This is another success as it shows that, to a reasonable degree of certainty, we can predict any of the aperture diameter, the pressure in the pumping chamber, or the flow rate, given the other two variables. This gives us the ability to design a system that will flow at virtually any rate, and to operate it successfully with only a minor amount of hassle. Furthermore, the success of these calculations implies that the pressures in the copper tubing, plotted in figure 3.2, are likely very close to being correct. This,

coupled with the likelihood that (3.18) is correct, indicates that the calculation we performed of the total relaxation due to magnetic field inhomogeneities is probably a fairly accurate prediction. So, we can gain some information about relaxation due to magnetic field inhomogeneities without actually introducing these inhomogeneities.

The success of the first two tests was not to be repeated in the third and last test, however. Once the pressure in the second cell had reached 50 torr, we attempted to find a signal in the cell. No signal was found. In fact, continued measurements at different pressures and at slightly different field strength showed no signal either. On the chance that the first charge of gas let into the second cell might have been overly contaminated with air, we pumped out the bottom cell and repeated the process. However, even after using many different field strengths and pressures of up to 142 torr, we continued to see absolutely no signal. As the electronics appeared to be working well, we concluded that virtually all of the polarization was lost in the travel down the tube. This test was not a complete failure however, as the healthy polarization in the pumping chamber indicted that the majority of the depolarization occurred between the aperture and the second cell. Given the less than ideal situation that we accepted in this region, there are many things to fix for further versions of this system. Firstly, a usable gold-plated hole can be acquired, and assiduously cleaned. Secondly, the flex fittings could be replaced with Ultratorr$^{\mathrm{TM}}$ connections. Thirdly, either a way to safely clean the copper tube could be found, or a different material could be used for the tubing, like the gold mentioned earlier in the thesis. Finally, in case the polarization loss were centered in the second cell itself, we could make sure that the cell was completely centered in the coils, in order to maximize T_2^*, and that pumping out the cell did not introduce too many impurities into it, perhaps by introducing a filter between the pump and the cell.

Chapter 6

Conclusion

Although no polarization was observed in the bottom cell after bleeding the polarized gas through both the 3.5 micron aperture and the thin copper tube, it would be hard not to call this experiment an overall success. Working from a well-balanced combination of theoretical prediction, experimental experience, and physical intuition, we were able to design and construct one of the first flowing-gas systems capable of maintaining a high degree of polarization in the pumping chamber. The creation of this system opens up the possibility of continually feeding polarized gas into a secondary container, whether it be the cyclotron ionization source, or the human lung. The ability to produce polarized ^{3}He theoretically for days at a time, without serious monitoring of the delivery system, would be invaluable in obtaining high quality measurements, such as required by the ^{19}Ne experiment mentioned back in Chapter one.

Constructing such a system would be beneficial by itself, but we went further with this thesis. The remarkable compliance of the measured flow rates to the calculated predictions leads us to believe that we may have a handle on both the dynamics of gas flow and the details of depolarization due to magnetic field inhomogeneities. Of course, only an experimental test measuring this relaxation will be conclusive, but what we have seen so far lends us confidence. The only negative at all was the lack

of a signal in the bottom cell, but that was by no means a disaster. There are many possible reasons as to why the signal might have disappeared, some of which were detailed at the end of the last chapter. Given the plethora of possibilities that could be implemented to improve on the design, which seems to work extremely well on the whole, it is likely that a solution to this problem will be found soon, and a signal will be seen in the bottom cell. Once this final step is reached, we will have built a polarized ^{3}He source for the Princeton Cyclotron, which is what we set out to do.

Appendix A

C Code

The entirety of the C code for the program pol.c that was referred to in Chapter 3 follows here:

```
#include <stdio.h>
#include <math.h>


#define Pp 0.1                    /* Pressure in plasma chamber */

#define M 3.25                    /* Atomic mass of helium-3 mixture */

#define disttoLf 12.06            /* Distance from tip of chimney

                                     to start of fixed volume */

#define Lf 86.36                  /* Length of fixed volume */

#define Pi 3.141592654            /* Pi */

#define Q  0.0253                 /* Throughput of 2 std cc/min */

#define Epsilon 0.000001          /* Accuracy of numerical solution */

#define Lc 138.50                 /* Length of capillary */

#define Dc 0.0254                 /* Diameter of capillary */

#define moldiam 2.61E-8           /* Molecular diameter of He-4

                                     (from Roth, pg. 31) */
```

```
#define gamma -2.034765086E4        /* Gyromagnetic ratio of He-3

                                       (scaled from the proton) */


double Pf, Pca, Pc, Pba, Pbb, Pb;  /* Reference pressures */
float dist[350], disterr[350];      /* Distance along tube with error */
float Bz[350], Bzerr[350];          /* Mag field along tube w/ error */
double Press[350];                  /* Pressures along tube */
int datanum, num1, num2, num3;      /* Reference data numbers */


double area(double diam);           /* Area of circle */
double pavisc(double press2, double ar, double temp);

                                       /* Viscous pressure through aperture */
double pamol(double press2, double ar, double temp);

                                       /* Molecular pressure through aperture */
double ptmol(double press2, double diam, double len, double temp);

                                       /* Molecular pressure through tube */
double ptvisc(double press2, double diam, double len, double temp);

                                       /* Viscous pressure through tube */
double prvisc(double press2, double s1, double s2, double len,
              double temp, double psai);

                                       /* Viscous pressure through rectangle */
double ptint(double press2, double ar, double len, double temp);

                                       /* Intermediate flow through tube */
double qtemp(double press1, double press2, double diam,
              double leng, double temp);

                                       /* Intermediate press through tube */
```

```
double pa_int(double press2, double ar, double temp);
                                    /* Intermediate pressure through aperture */
void magread();                /* Reading magnetic field and distance data */
void pressout(double temp, double diam);
                                    /* Pressure calculation */
double gasrelax(double temp, double diam);
                                    /* Gas relaxation calculation */
double lambda(double press, double temp);
                                    /* Mean free path calculation */


void main(void)                    /* Calls relevant functions */
{
 int i, j;                         /* Counters */
 float Bzplus = 10.0;              /* Additional magnetic field */
 double T = 303.14;                /* T set to room temperature */
 double Df;                        /* Inner diameter of fixed length */
 double gsre=0.0;                  /* Polarization relaxation */

 magread();                        /* Reads magnetic field data */
 for (i=0; i<=datanum; i++) Bz[i]+=Bzplus;
                                    /* Adds additional field */
 Df=0.0254;                        /* Sets diameter of fixed length*/

 pressout(T, Df);                  /* Calculates pressures */
 gsre=-100.0*gasrelax(T, Df);      /* Calculates gas relaxation */
```

```c
  printf("at %f K, %f cm Df, and %f additional magnetic field
        gives a loss in polarization of %g %%\n", T, Df,
        Bzplus, gsre);
}


void pressout(double t, double d) /* Calculates Pressures */
{
 int i;                              /* Counter variable */
 double ETA, PDi, Da;               /* Viscosity, intersection point,
                                        diameter of aperture */


 for (i=0; i<=datanum; i++)         /* Initializes pressures */
   Press[i]=0.0;
 Pf=Pca=Pc=Pb=0.0;


 ETA=(12.570E-6)*pow(t, 0.5)/(1+79./t);
                                    /* Viscosity (scaled from 186E-6 via
                                        Roth (2.72)) */
 PDi=116*pow((t/M), 0.5)*ETA;       /* Intersection point (Roth (3.227)) */


 Pf=pamol(Pp, area(d), t);          /* Pressure at start of fixed length */


 for (i=0; i<num1; i++) Press[i]=Pp;


 for (i=num1; i<num2; i++)          /* Determines the regime and
                                        calculates pressures within
```

```
                              fixed length */
    {

      if (Press[i-1]>(10.*PDi/d))

        Press[i]=ptvisc(Pf,area(d),(double) ((dist[0]-disttoLf)-dist[i]),t);

      else if (Press[i-1]<(0.1*PDi/d))

        Press[i]=ptmol(Pf,d,(double) ((dist[0]-disttoLf)-dist[i]),t);

      else

        Press[i]=ptint(Pf,d,(double) ((dist[0]-disttoLf)-dist[i]),t);

    }


if (Press[num2-1]>(10.*PDi/d))

  {

    Pca=Press[num2-1];

    Pc=pavisc(Pca, area(d), t);

  }
else if (Press[num2-1]<(.1*PDi/d))

  {

    Pca=Press[num2-1];

    Pc=pamol(Pca, area(d), t);

  }
else

  {

    Pca=Press[num2-1];

    Pc=pa_int(Pca,area(d),t);

  }
```

```
for (i=num2; i<=datanum; i++)    /* Pressures for capillary

                                        in viscous regime */

  {

    Press[i]=ptvisc(Pc, area(Dc), (double)

                  ((dist[0]-disttoLf-Lf)-dist[i]),t);

  }

Da=3.0E-4;                          /* Sets diameter of aperture */

Pba=ptvisc(Pc, area(Dc), Lc, t); /* Pressure before aperture */


Pbb=pavisc(Pba, area(Da), t);    /* Pressure in pumping chamber */

    /* This line calculates pressure in pumping chamber with

       a rectangular aperture; we do not use it here.

       Pb=prvisc(Pba, 5.0E-5, 1.9875E-2, 1.27, t, 0.002); */


printf("A ballast pressure of %g Torr ", Pbb);

}



double area(double di)           /* Calculates area */

{

  double A;


  A = (Pi/4)*pow(di, 2);

  return A;

}
```

```
double pavisc(double p2, double a, double te)
                                    /* Calculates viscous pressure through */
{                                   /*  an aperture (solution of
                                        Roth (3.30-1)) */
  double pav;


  pav = p2/2 + (pow(((4*pow(p2,3)*pow(Q,5)*pow((5*te/M),(2.5))
        *pow((9.13*a),5))+(pow(p2,8)*pow((5*te/M),5)
        *pow((9.13*a),10))),0.5))/(2*pow(p2,3)*pow((5*te/M),(2.5))
        *pow((9.13*a),5));


  return pav;
}


double pamol(double p2, double a, double te)
                                        /* Calculates molecular pressure through */
{                                       /*  an aperture (Roth (3.72)) */
  double pam;


  pam = Q/(3.64*a*pow(te/M, 0.5))+p2;


  return pam;
}


double ptmol(double p2, double d, double l, double te)
```

```
                                          /* Calculates molecular pressure */
{                                         /*  through a tube (Roth (3.93)) */
  double ptm, ctmo;


  ctmo = 3.81*pow(te/M, 0.5)*pow(d, 3)/l;

  ptm = Q/ctmo + p2;

  return ptm;

}



double ptvisc(double p2, double a, double l, double tem)

                                      /* Calculates viscous pressure */
{                                     /*  through a tube (Roth (3.50-2)) */
  double ptv, ETA;


  ETA=(12.5702E-6)*pow(tem, 0.5)/(1+79./tem);

  ptv = pow(((Q*(37.728)*ETA*l / pow(a, 2.0)) + pow(p2, 2)), 0.5);

  return ptv;

}



double prvisc(double p2, double si1, double si2, double l,

                              double tem, double psi)

                              /* Calculates viscous pressure through

                                 a rectangular aperture

                                 (Roth (3.63, fig 3.9)).

                                 Not used in final configuration */

{
```

```
   double ptv, ETA;


   ETA=(12.5702E-6)*pow(tem, 0.5)/(1+79./tem);

   ptv = pow(((Q*(18.0382)*ETA*l / (psi*si1*pow(si2, 3.0)))

         + pow(p2, 2)), 0.5);

   return ptv;

}


double ptint(double p2, double d, double l, double te)

                                       /* Calculates intermediate pressure */

{                                      /*  through a tube (Roth (3.221-3.239)) */

   double pti;

   double p1, step;

   int i;


   p1=0;


                                       /* Approximates solution of Roth (3.233)

                                          by looking for a root within

                                          decreasing intervals */

   for (step=100.; step >= Epsilon; step = step/10.)

     {

       for (i=0; i<=9; i++)

 if ((qtemp(p1+i*step, p2, d, l, te) -Q <= 0.)

            && (qtemp(p1+(i+1)*step, p2, d, l, te) - Q >= 0.))

     {
```

```
        break;
    }
        p1=p1+i*step;
    }


  pti=p1;


  return pti;
}


double qtemp(double pr1, double pr2, double di, double len, double tem)
  {                                   /* Calculates throughput of intermediate
                                         flow through a tube (Roth (3.233)) */
    double ctmo, delta, qte, PDi, ETA;


    ETA=12.5702E-6*pow(tem, 0.5)/(1+79./tem);
    PDi=116*pow((tem/M),0.5)*ETA;
    ctmo = 3.81*pow(tem/M, 0.5)*pow(di, 3)/len;
    delta = (pr1)*di/(2*PDi);


    qte = (ctmo*PDi/di)*((.5)*pow(delta,2)
        +(17./21.)*delta+(.009)*log(1+(21.)*delta));


    return qte;
  }
```

```c
double pa_int(double pr2, double ara, double te)
{                                       /* Calculates intermediate pressure

                                           through an aperture using an

                                           average of visc and mol pressures */

  double pai, paiv, paim;


  paiv=pavisc(pr2,ara,te);

  paim=pamol(pr2,ara,te);


  pai = .5*paiv + .5*paim;

  return pai;

}



void magread()                          /* Reads magnetic field data in from */
{                                       /*  file magfld1.dat */

  FILE *magfld;


  int i;

  float *pd, *pb, *pde, *pbe;

  pd=dist, pb=Bz, pde=disterr, pbe=Bzerr;

  magfld=fopen("magfld1.dat", "r");


  for(i=0; i<= 350; i++)                /* initializes arrays */

    dist[i]=Bz[i]=disterr[i]=Bzerr[i]=0.0;


  while (fscanf(magfld, "%f %f %f %f", pd++, pb++, pde++, pbe++) > 1)
```

```
    datanum++;
  datanum -= 1;                       /* Eliminates end of file marker */


  for (i=0; i<=datanum/2; i++)    /* Loop reverses order of arrays */
    {
      double temp1, temp2, temp3, temp4;


      temp1=dist[i], temp2=Bz[i];
      temp3=disterr[i], temp4=Bzerr[i];
      dist[i]=dist[datanum-i], Bz[i]=Bz[datanum-i];
      disterr[i]=disterr[datanum-i], Bzerr[i]=Bzerr[datanum-i];
      dist[datanum-i]=temp1, Bz[datanum-i]=temp2;
      disterr[datanum-i]=temp3, Bzerr[datanum-i]=temp4;
    }
  for (i=0; (dist[0]-dist[i]) < disttoLf; i++) num1++;
  for (i=0; (dist[num1]-dist[i])<Lf; i++) num2++;
  num3=num2;
  for (i=num2; i<=datanum; i++)
    {
      if ((dist[0]-disttoLf-Lf-dist[i])<=Lc) num3++;
    }
}


double gasrelax(double t, double d)

                                /* Calculates relaxation time of He-3 */

{
```

```
int i;

double overT1[350];                  /* Inverse of relaxation time */

double gradBz[350];                  /* Magnetic Field Gradient */

double D[350];                       /* Effective diffusion constant */

double spd[350];                     /* Speed of gas down tube */

double pol=0.0;                      /* Polarization loss */


for (i=0; i<=datanum; i++)        /* Initializes arrays */
  gradBz[i]=D[i]=spd[i]=overT1[i]=0.0;


gradBz[0] = (Bz[0]-Bz[1])/(dist[0]-dist[1]);

                                     /* Calculates magnetic field gradients */
gradBz[datanum] = (Bz[datanum-1]-Bz[datanum])
               /(dist[datanum-1]-dist[datanum]);
for (i=1; i<=datanum-1; i++)
  gradBz[i]=((Bz[i-1]-Bz[i])/2.+(Bz[i]-Bz[i+1])/2.)
          /((dist[i-1]-dist[i])/2.+(dist[i]-dist[i+1])/2.);


for (i=0; i<=datanum; i++)         /* Calculates effective diffusion
                                      constants taking into account
                                      maximum mean free path and using
                                      (37) of Gamblin&Carver */
  {
    double vav=(1.45E4)*pow((t/M), (0.5));
                                     /* Average velocity of gas
```

```
                                        molecules (Roth (2.42)) */
    double l=lambda(Press[i],t);


    if (i<num2 && l<=d/2)

      D[i]=(1/2.13)*(l*vav)

          /(1+pow((gamma*Bz[i]), 2)*pow((l/vav), 2));
    else if (i<num2 && l>d/2)

      D[i]=(1/2.13)*(d/2*vav)

          /(1+pow((gamma*Bz[i]), 2)*pow(((d/2)/vav), 2));
    else if (i>=num2 && i<=num3 && l<=Dc/2)

      D[i]=(1/2.13)*(l*vav)

          /(1+pow((gamma*Bz[i]), 2)*pow((l/vav), 2));
    else if (i>=num2 && i<=num3 && l>Dc/2)

      D[i]=(1/2.13)*(Dc/2*vav)

          /(1+pow((gamma*Bz[i]), 2)*pow(((Dc/2)/vav), 2));
    else D[i]=0.0;
  }
                                        /* Calculates inverse of relaxation */
for(i=num1; i<=num3; i++)            /* time from (37) of Gamblin&Carver */
  overT1[i]=(0.5)*D[i]*pow(gradBz[i], 2)/pow(Bz[i], 2);



for(i=num1; i<=num3; i++)            /* Calculates speed of gas down tube */
  {
    if (i<num2)

      spd[i]=Q*1000/(Press[i]*area(d));
```

```
    else if (i>=num2)

      spd[i]=Q*1000/(Press[i]*area(Dc));

  }

                                    /* Integrates inverse of relaxation time

                                       over time spent in tubes to obtain

                                       the total loss of polarization */

pol += -overT1[num1]*(dist[num1]-dist[num1+1])/(spd[num1]);

pol += -overT1[num3]*(dist[num3-1]-dist[num3])/(spd[num3]);

for(i=num1+1; i<num3; i++)

pol += -overT1[i]*((dist[i-1]-dist[i])/2.+(dist[i]-dist[i+1])/2.)/spd[i];


return pol;

}


double lambda(double p, double te)

                                    /* Calculates the mean free path

                                       (Roth(2.57)) */

{

  double lmbda;


  lmbda = (2.33E-20)*te/(pow(moldiam, 2.0)*p*(1+79/te));


  return lmbda;

}
```

Bibliography

[1] *Handbook of Chemistry and Physics*. CRC Press, 1990.

[2] E. G. Adelberger and W. C. Haxton. Parity violation in the nucleon-nucleon interaction. *Ann. Rev. Nuc. Part. Sci.*, 35, 1985.

[3] E. G. Adelberger, H. E. Swanson, M. D. Cooper, W. Tape, and T. A. Trainor. *Phys. Rev. Lett.*, 34, 1975.

[4] P. L. Anthony et al. Determination of the neutron spin structure function. *Physical Review Letters*, 71(7), 1993.

[5] G. D. Cates, F. P. Calaprice, and R. B. Vogelaar. Nsf proposal for a program based on the use of the princeton cyclotron. Technical report, Princeton University, 1994.

[6] G. D. Cates, D. J. White, Ting-Ray Chien, S. R. Schaefer, and W. Happer. Spin relaxation in gases due to inhomogeneous static and oscillating magnetic fields. *Physical Review A*, 38(10), 1988.

[7] T. E. Chupp, M. E. Washgul, K. P. Coulter, A. B. McDonald, and W. Happer. Polarized, high-density, gaseous ^{3}He targets. *Physical Review C*, 36(6), 1987.

[8] T. B. Clegg. An electron-cyclotron-resonance ionizer for $^3\vec{he}$. In R. W. Dunford and F. P. Calaprice, editors, *Workshop on Polarized ^{3}He Beams and Targets*, pages 25–28. American Institute of Physics, New York, 1985.

[9] B. Deplanques, J.F. Donoghue, and B. R. Holstein. *Ann. Phys.*, 129, 1980.

[10] Roger L. Gamblin and Thomas R. Carver. Polarization and relaxation processes in ^{3}He gas. *Physical Review*, 138(4A), 1965.

[11] W. Happer, E. Miron, S. Schaefer, D. Schreiber, W. A. van Wijngaarden, and X. Zeng. Polarization of the nuclear spins of noble-gas atoms by spin exchange with optically pumped alkali-metal atoms. *Physical Review A*, 29(6), 1984.

[12] D. P. May and S. D. Baker. The polarized ^{3}He beam on the texas a&m cyclotron. In R. W. Dunford and F. P. Calaprice, editors, *Workshop on Polarized ^{3}He Beams and Targets*, pages 1–7. American Institute of Physics, New York, 1985.

[13] H. Middleton, R.D. Black, B. Saam, G. D. Cates, G. P. Cofer, R. Guenther, W. Happer, L. W. Hedlund, G. A. Johnson, K. Juvan, and J. Swartz. Mr imaging with hyperpolarized ^{3}He gas. *Magnetic Resonance in Medicine*, 1994.

[14] Alexander Roth. *Vacuum Technology*, pages 1–121. North-Holland Publishing Company, Amsterdam, 1976.

[15] Brian Saam. *Pulse-NMR Studies of Spin Relaxation Relevant to Laser-Polarized Noble Gases*. PhD thesis, Princeton University, 1995.

[16] L. D. Schearer and G. K. Walters. Nuclear spin-lattice relaxation in the presence of magnetic-field gradients. *Physical Review*, 139(5A), 1965.